TOPICAL REVIEW • OPEN ACCESS

Infrared thermography for boundary layer transition measurements

OPEN ACCESS
IOP Publishing
Measurement Science and Technology
Meas. Sci. Technol. **31** (2020) 112002 (21pp)
https://doi.org/10.1088/1361-6501/aba070

Infrared thermography for boundary layer transition measurements

C Christian Wolf, Anthony D Gardner and and Markus Raffel

Institute of Aerodynamics and Flow Technology, German Aerospace Center (DLR), Bunsenstr. 10, Göttingen, Germany

E-mail: Christian.Wolf@DLR.de

Received 22 April 2020, revised 13 June 2020
Accepted for publication 26 June 2020
Published 23 September 2020

Abstract

Infrared thermography has been successfully adopted in the field of flow diagnostics over the last decades. Detecting the laminar–turbulent boundary layer transition through variations in the convective heat transfer is one of the primary applications due to its impact on the aerodynamic performance. Recent developments in fast–response infrared cameras allow unsteady measurement of fast–moving surfaces and moving transition positions, which must consider the thermal responsiveness of the surface material. Experimental results on moving boundary layer transition positions are highly valuable in the design and optimization of airfoils or rotor blades in unsteady applications, for example regarding helicopter main rotors in forward flight. This review article summarizes recent developments in steady and unsteady infrared thermography, particularly focusing on the development of differential infrared thermography (DIT). The new methods have also led to advances in the analysis of unmoving boundary layer transition for static airfoil test cases which were previously difficult to analyze using single–image methods.

Keywords: boundary layer, laminar-turbulent transition, infrared thermography, unsteady aerodynamics

(Some figures may appear in colour only in the online journal)

1. Introduction and scope

The laminar–turbulent transition of the boundary layer (BL) is one of the key factors when optimizing the aerodynamic performance of vehicles, referring to large drag penalties due to different skin friction coefficients, or referring to the impact of the BL parameters on the stall resistance. The measurement, prediction, and manipulation of the BL was tackled in numerous studies concentrating on steady aerodynamics with a stationary transition position, as found on fixed–wing aircraft, road vehicles, trains, etc

Unsteady inflow conditions result in complex aerodynamics and a moving transition location, as for example seen on helicopter main rotor blades in forward flight. The superposition of rotational and freestream velocities, and the consequent cyclic swashplate input to achieve moment trim, produce periodic variations of both the inflow magnitude and inflow direction at a given radial cross–section. It is known from simulations in steady hovering conditions that modeling of the BL transition is crucial for a correct prediction of the rotor power requirement, for example see Egolf *et al* [1]. Therefore, several contributions were made to integrate transition models into computational fluid dynamics over the last decades (Beaumier and Houdeville [2], Beaumier *et al* [3], Zografakis *et al* [4], Coder [5]). More recently, Heister [6] implemented several empirical criteria (Tollmien–Schlichting and crossflow instabilities, bypass mechanisms, and attachment line contamination) into an URANS framework provided by the DLR TAU Code. A similar approach was chosen by Richez *et al* [7] for the ONERA *elsa* code. Both studies performed successful comparisons to experimental data of the 7A/7AD rotor taken from integral torque measurements or point wise hot–film sensors applied within the GOAHEAD

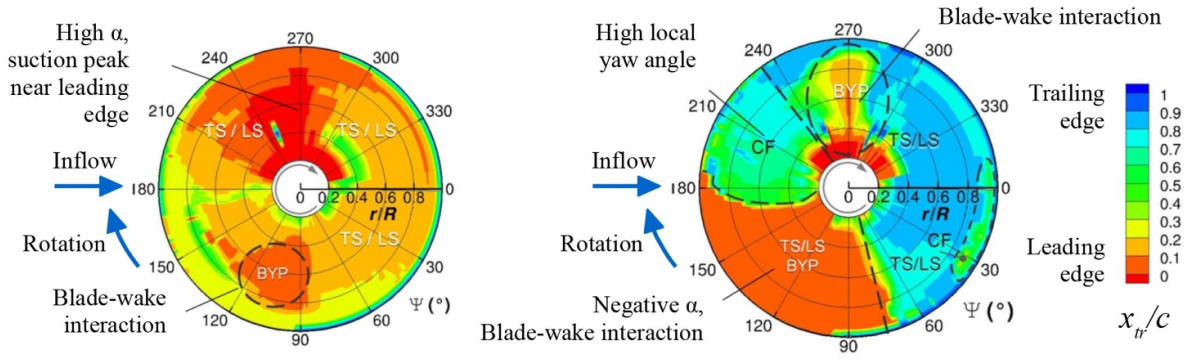

Figure 1. Prediction of the transition location x_{tr} on the upper (left) and lower (right) side of a trimmed rotor in forward flight, reproduced from Heister [6].

project [8]. However, a conclusive validation of numerical tools would benefit from spatially well–resolved experimental data including three–dimensional effects, which is apparent from the predicted transition distributions shown in figure 1 for a trimmed rotor at an advance ratio of 0.33.

For turbomachinery aerodynamics, an unsteady inflow of the compressor or turbine blades in a rotor–stator layout is caused by the periodic wake of preceding stages, which also results in moving BL transition [9, 10]. The transition not only affects the friction drag, but also the thermal loads of the blades. It is particularly difficult to access this type of flow with sensors and measurement equipment, hence, many studies simplified the setup by investigating the influence of periodic inflow perturbations on flat plates [11, 12], curved surfaces [13], or stationary blade cascades [14]. In addition, early fundamental research of moving BL transition on flat plates [15, 16] has currently been reviewed for fixed–wing aircraft applications [17], assuming that low–frequency atmospheric turbulence may affect the performance of natural laminar–flow airfoils.

The blades of horizontal–axis wind turbines can easily be subject to unsteady aerodynamics due to wind shear effects, yaw angles, interactions with the tower, or aeroelasticity [18, 19]. It can be expected that these unsteady effects become increasingly important in the future, given that the laminar flow length is a crucial parameter of wind turbine airfoil design [20]. Another recent publication by Thiessen and Schülein [21] concentrated on moving transition positions due to the effect of forward flight velocity on a fixed–pitch propeller for unmanned aerial vehicles.

Steady BL transition over a wetted surface can be measured by techniques which are well–known and understood. There are several experimental methods available, with infrared thermography (IRT) being one of the most convenient and most popular methods. IRT is non–intrusive and produces spatially resolved results in a two–dimensional measurement domain. No instrumentation of the model is required, but in some cases, an insulating surface coating must be applied depending on the base material. Pioneering work as described by Quast [22], Carlomagno *et al* [23], or de Luca *et al* [24] developed the underlying principle based on the Reynolds analogy. A small difference between the surface temperature T_w and the fluid temperature T_∞ yields a convective heat flux $\dot{q}$ depending on the local skin friction coefficient C_f,

$$\dot{q} = \frac{C_f}{2} U_\infty \frac{\lambda}{\nu} (T_w - T_\infty), \tag{1}$$

with the external flow velocity U_∞, and the fluid's thermal conductivity λ and kinematic viscosity ν. The surface temperature T_w additionally depends on the conductive and radiative terms, but a qualitative evaluation of the surface temperature distribution T_w is usually sufficient to differentiate between the laminar and turbulent regions of the BL. This also means that a temperature calibration of the camera, depending the surface emissivity and the heat flux sensor as described by Astarita and Carlomagno [25], is not mandatory. The current work will partly use the raw infrared signal in arbitrary camera units ('counts') as synonym for the surface temperature. In recent years IRT has become a standard tool for the detection of static transition positions. It was applied in wind tunnel testing of airfoils [26, 27] or fixed–wing models [28], supersonic transition measurements [29, 30], and in–flight measurements [31, 32].

The current paper reviews recent developments of unsteady infrared thermography applied to moving boundary layer transition measurements in unsteady inflow conditions. In particular, the development of the differential infrared thermography (DIT) at the German Aerospace Center (DLR) in Götingen is covered in chapter 4 and illustrated with examples and applications in the field of helicopter rotor aerodynamics. The background to these activities is given by a summary of other unsteady but non–infrared methods in chapter 2, and a summary of steady infrared thermography in chapter 3 which is the basis for unsteady measurements. Detailed considerations of infrared radiation physics or camera technologies, see [25, 33], or infrared applications on other aerodynamic topics, such as heat flux measurements for super- and hypersonic applications [34], are beyond the current scope.

2. Non–infrared methods for unsteady transition positions

2.1. Hot-film sensors

The hot–film is a flush–mounted surface sensor that uses the principle of constant temperature anemometry similar to the

well–known hot–wires. It is a standard method for measuring the wall shear stress over the Reynolds analogy for heat transfer, also see equation (1), in a boundary layer [35, 36]. It can be used to detect dynamically moving boundary layer transition [37], but can also distinguish between transition, stagnation point motion, flow separation, and shock formation [38]. The state of the literature for transition measurements on static airfoils with non-moving transition is particularly good, see for example [39]. It should be noted that much of this literature refers to the unsteady turbulent structures within the BL, see for example [40], rather than a dynamically moving boundary layer position as experienced by the pitching airfoil or the helicopter rotor in forward flight.

The pitching airfoil has been investigated for low–Mach number airfoils [41–43] and for helicopter–relevant airfoils at Mach with compressible flow [38, 44, 45]. The investigations of Richter *et al* involve 50 sensors on each airfoil, and are suitable for CFD calibration, see the comparisons in [46]. Hot–film sensors have also been extensively used for the investigation of dynamically moving BL transition on laminar airfoils [47, 48], particularly in relation to aeroelastic flutter. Lorber and Carta [49] did extensive investigations of the BL transition and flow separation on a pitching airfoil, but the transition investigations involved only two sensors due to the low chordwise resolution. For the rotating system, Sémézis [50] performed a hot–film investigation on the 7AD rotor and investigations within the GOAHEAD project [8]. The data was also used for CFD validation [6]. A similar BL transition measurement using hot–films on an instrumented full–scale wind turbine blade was done by Schaffarczyk *et al* [51].

The evaluation of hot–film data presents several difficulties, which have increasingly been identified and at least partially solved in recent years. The first major problem is that for a dynamically moving BL transition, the transition intermittency is no longer seen as a transient stepping function. For a stationary BL transition region, a series of turbulent spots is generated and propagates past each sensor, and the fraction of time in which the sensor is in the laminar or turbulent state is the experimentally defined intermittency. For the moving boundary layer, an increased RMS signal is present, but the intermittency signal never appears, leaving the transition position to be assessed through the soft step attained between laminar and turbulent flow [52]. The step assessment also lends itself to fully automated data processing (through data skew), which solves the second problem of dealing with the large amount of data required to include the sensor cut–off frequencies of around 60 kHz [37, 52].

An additional problem of hot–film sensors is that they involve an intrusion into the flow. Even if the sensor carrier foil is carefully kept to the same contour as the airfoil, the different surface roughness can result in a difference in the transition position, see figure 2. For the same reason, the edges of the foil and the localized heating spots of the sensors may cause disturbances. These influences can be reduced through good design and careful construction, but they can never be completely avoided. Similarly, Mertens *et al* [53], noted that the regions of a pitching airfoil with pressure sensors had measurably different boundary layer transition for some test cases, either due to the local surface heating, or the pressure taps.

For impulsive, particularly hypersonic test facilities, the hot–film gauges can be operated in an unheated mode, and are called thin–film gauges, see for example [54]. In this case the 'cold' resistance of the sensor is related to the heat transfer from the wall. The gauges have reaction times of the order of microseconds, but to the authors' knowledge were not yet used for dynamically moving boundary layer transition. An alternative to hot–films is to place hot–wires in the BL flow, and indeed these offer advantages for some flow topologies, especially for wake investigations [55] or for a rotating axisymmetric cone [56].

2.2. Pressure sensors and microphones

The σC_P–method analyzes pressure signals from fast–response surface pressure transducers [57]. If the pressure sensor signals are evaluated for an airfoil's periodic pitch motion, then the differences between different cycles will be low in the laminar flow regions, medium in turbulent regions, and a maximum near the transition position. This is because slight differences in the wind tunnel operating conditions or the pitch mechanism result in small cycle–to–cycle variations of the moving transition position. Hence, in a certain phase of the cycle, the transition position is in front of a given pressure sensor for some cycles but behind the sensor for the other cycles. This increases the cycle–to–cycle standard deviation of the pressure, σC_p, since the transition affects the BL displacement thickness. A sample analysis of a pressure transducer mounted to the suction surface of a rotor blade at 19% chord is shown in figure 3. Due to the chosen cyclic pitch amplitude, both the BL transition and the BL separation inducing dynamic stall leave a footprint in the standard deviation of C_p.

The σC_p–technique does not require a very high temporal resolution of the pressure sensor as long as the overall aerodynamics is properly captured. This is due to the fact that no boundary layer modes are identified, but only the motion of the transition position which is a broadband signal. The method has been demonstrated for pitching airfoils at both high and low inflow velocities [57, 59], and for pitching finite wings in both swept and unswept configurations [60, 61]. An application to a rotor with cyclic pitch is also possible [62, 63] but the sensor integration requires additional effort, for example by means of a telemetry system. Gao *et al* [64] and Wei *et al* [65] proposed an approach which is similar to the σC_p–idea but was developed independently. In their case, it was shown that using a sliding window analysis rather than the cycle–to–cycle deviation yields transition results with a comparable quality. Another evaluation strategy in literature is the M–TERA intermittency approach. It was originally formulated for velocity fluctuations [66], but recently adapted to surface pressure fluctuations and transient inflow conditions [17]. The method must be seen as requiring additional validation.

Microphones with a much broader frequency response than the subsurface pressure sensors can also be used to detect BL transition, see [67, 68]. Microphones allow an analysis of boundary layer frequencies or modes of interest in addition to

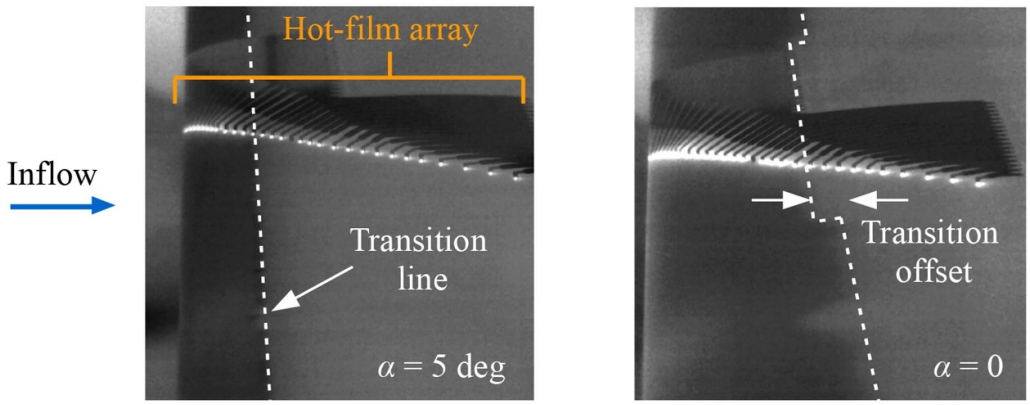

Figure 2. Infrared images showing a difference of the transition position due to the presence of a hot–film foil, adapted from Richter *et al* [46].

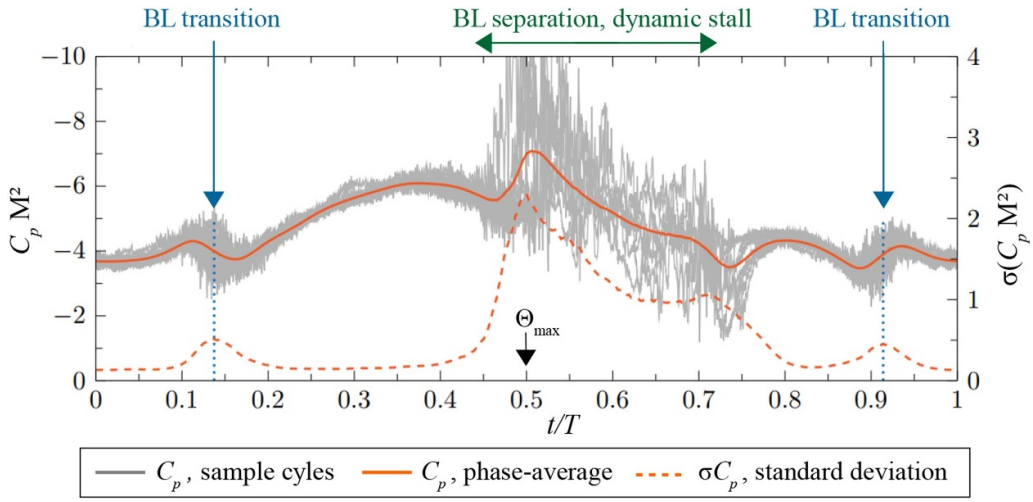

Figure 3. σC_p–analysis for a rotor blade with cyclic pitch input, $f = 23.6$ Hz, pitch amplitude $\hat{\Theta} = 6°$, adapted from Schwermer [58].

the mere transition location, but with additional difficulties in analyzing the acoustics.

2.3. Temperature–sensitive paint

Temperature–sensitive paint (TSP) is used in many of the same situations where infrared thermography can also be applied [69]. Under cryogenic conditions, TSP proved to be beneficial [70] in contrast to IRT due to the challenges of capturing the reduced radiated energy in the infrared spectrum [71]. The surface preparation with the delicate paint layer requires additional effort, and it offers the disadvantage that the surface contour may be altered. The surface roughness of the TSP can be very low if polished [72]. The data acquisition using optical cameras allows a higher resolution compared to infrared cameras, which enables a precise image dewarping and a tracking of small-scale aerodynamic features. TSP can be used for very short time exposures, see [73, 74]. The use of difference–image techniques allows the use of TSP for the detection of dynamically moving BL transition, as applied on a slowly moving model during a pitch sweep test [75], but yet to be demonstrated on dynamically oscillating models.

2.4. Direct skin friction measurements

Direct skin friction measurements provide the most desirable data for any boundary layer problem. A possible approach is using sunk piezoelectric balances on which a small surface (‘movable wall element’) is mounted. The acquisition of a moving boundary layer transition seems feasible, since small–floating mass, fast-response gauges are possible [76]. However the practical difficulty of achieving the precise tolerances and low noise for this measurement mean that not much data is available [77], and have not yet been used for moving boundary layer transition. The sensors also have a temperature and acceleration sensitivity which must be compensated. Another method of skin friction measurement is given by shear–sensitive liquid crystals [78], but these have also not yet been used for dynamically moving boundary layer transition.

2.5. Comparison of different methods

Table 1 provides a short comparison of the most important measurement techniques for unsteady BL transition positions, listing their main advantages and disadvantages, and providing guidelines for the design of future experiments. Note that

Table 1. Main advantages and disadvantages of unsteady measurement techniques.

Method	Advantages	Disadvantages
Hot–film sensors	• Well–established and well–understood measurement principle • Very high frequency range provides deeper insight into the flow beyond transition position • Suitable as reference for optical measurement techniques • Automated data analysis techniques available, but different from steady–state analysis	• Extensive model preparation required, particularly for rotating surfaces (telemetry or on–board systems) • Careful preparation of the experiment required (bridge balancing etc.) • Surface roughness and introduced heat probably affect flow • Low spatial resolution
Pressure sensors	• Transition detection is a by–product of measuring pressure or lift distributions • Suitable as fast–response reference for optical measurement techniques • Post–processing of acquired data is simple and can be automated • Broadbanded response, robust to filtering	• Extensive model preparation with careful sensor layout required, particularly for rotating surfaces • Subscale models require miniaturized sensors, often with limited or no possibilities for sensor repair • Low spatial resolution • Pressure tap affects BL transition
Temperature sensitive paint	• 2D measurement with very high resolution possible • Camera and optics equipment less costly than IR cameras • Surface coating can be polished for very low surface roughness	• Surface coating on the order of 100 μm required • Methods for unsteady measurements under development, may require validation with reference technique
Unsteady infrared techniques	• Comparably low effort for experimental setup and model preparation • Particularly suitable for full–scale applications • Non–intrusive technique • 2D measurements with high resolution (but usually lower than TSP) possible	• Additional thermal measurement lag • Requires temperature difference between surface and flow, i.e. heating • Infrared spectrum is susceptible to reflections from the measurement environment • Comparably new technique, may benefit from comparison to reference sensors

fast–response infrared techniques to be discussed in chapter 4 are already included for the sake of completeness.

3. Infrared thermography (IRT) for steady transition positions

In comparison to other methods IRT enables convenient and two–dimensional measurements of the BL transition location. Therefore, IRT is particularly suitable for full–scale in–flight measurements, as demonstrated by Horstmann *et al* [79] or Crawford *et al* [31, 32] on general aviation aircraft. With a view to unsteady measurements in the following chapter, this section concentrates on applications with a stationary transition location due to steady inflow but fast–moving, particularly rotating surfaces.

The basic IRT setup consists of an infrared camera, a strategy to achieve a fluid–surface temperature difference as required by equation (1), and, if needed, a surface preparation. The temperature difference can be achieved through:

- Surface heating by external radiation flux sources: general purpose spotlights [63, 80], infrared emitter [81], infrared laser [21], or sunlight [68, 82].
- Surface heating by internal resistance heating: electrically conductive paint [83], carbon nano tube materials [84], heat foils [81], etc.
- Surface pre–heating [85, 86] or pre–cooling [82] for short–term tests.
- Inflow temperature: temperature–controlled laboratories or wind–tunnels, altitude changes during atmospheric flight [32], etc.

The required temperature difference is often reported to be on the order of several Kelvin but it depends on the setup and the resulting signal–to–noise ratio, and no general recommendations can be made. The transition position itself may be

affected if the heating is too strong, see Joseph *et al* [26] and Costantini *et al* [87] for further recommendations.

An insulating and dull coating can be applied to the surface in order to reduce the thermal conductivity and to maximize the infrared emissivity [25], which is mandatory for metallic surfaces but optional for carbon fiber reinforced plastics. Fiducial markers with differing radiation properties, for example silver conductive paint, can be used to register and dewarp the infrared images.

The inherent motion blur in the infrared images must be considered if a fixed ground–based camera is used to observe fast–moving rotor blades. To the authors' knowledge, no infrared camera placement within the rotating frame has yet been realized. Hub–mounted rotating cameras for the visible light spectrum have been demonstrated [88, 89], requiring a miniaturized camera size, a high tolerance towards centrifugal forces, and a high resolution to perform image dewarp under oblique viewing angles.

Current infrared cameras are based on either thermal detectors, which sense the incident energy flux, or quantum detectors, which absorb incoming photons [25, 33]. The former principle can, for example, be realized using mircobolometer arrays, which is the cost–effective standard choice for many cameras applied to steady–state BL measurements. The required image exposure times are in the range of several milliseconds [90] and, therefore, unsuitable to 'freeze' the motion of rotor blades. Quantum detectors are used in high–speed infrared cameras, featuring both a high repetition rate ($f > 100$ Hz) and small image exposure times ($\Delta t < 100 \mu s$). The sensor resolution is currently between about 0.2 Mpx and 0.5 Mpx, which is at least one order of magnitude smaller than today's visible–light cameras. The signal–to–noise ratio of the infrared images depends on the surface emissions, the camera exposure time, and its noise–equivalent temperature difference (NETD), which is typically below 50 mK. The majority of the studies discussed in the following sections were conducted using either mercury cadmium telluride (MCT) or strained layer superlattice (SLS) sensors, both sensitive in the long–wave infrared band (LWIR), or indium antimonide (InSb) sensors, sensitive in the mid-wave infrared band (MWIR). In practice LWIR can be advantageous over MWIR since carbon fiber surfaces are opaque in the long–wave regime and require no additional surface treatment.

Reichstein *et al* [68] successfully performed BL transition measurements on a 2 MW–wind turbine spinning at up to 9 rpm, combining ground–based infrared cameras of both MCT and InSb types with blade–mounted microphones. The viewing distances of the cameras were 80 m and 140 m, with image exposure times of about 100 μs. It is noted that many large–scale measurements are limited by the scarce availability and high costs of telescopic lenses for infrared cameras. Reichstein *et al* only observed small laminar flow lengths on the blade's suction side during nominal operation conditions of the wind turbine, but larger laminar lengths occurred during the transient spin–up of the rotor due to lower Reynolds numbers. A similar investigation was conducted by Dollinger *et al* [91]. Other wind turbine–related research focusing on infrared on–site monitoring of structural blade defects found

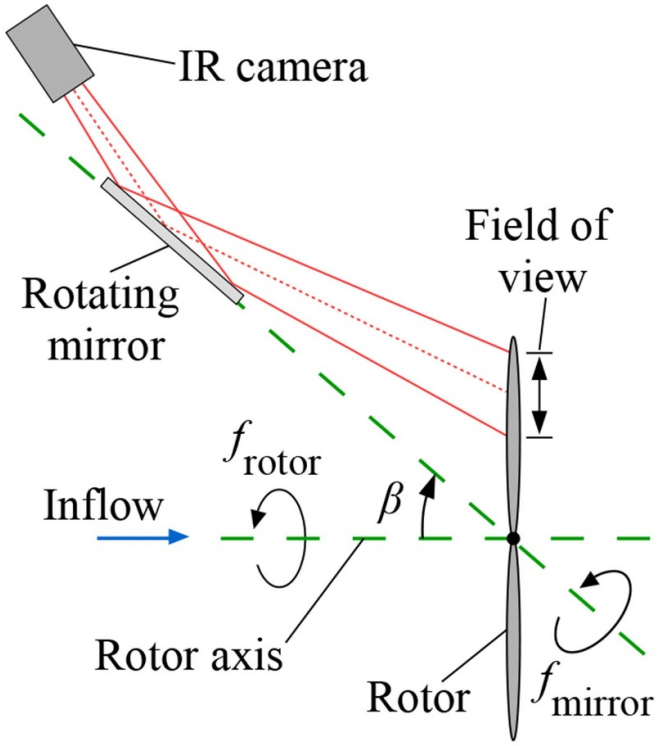

Figure 4. Infrared image derotation in off–axis geometry [93].

BL transition wedges due to leading edge erosion as a by–product [92].

The rotational frequency of rotors or propellers for aircraft applications is large in comparison to wind turbines, particularly when investigating sub–scale models. The corresponding motion blur can be reduced or avoided by optical blade tracking, as an additional measure complementing short–exposure cameras. Rotating mirrors are suitable for this purpose if the rotor hub position is stationary in a laboratory or wind–tunnel environment. Several options for different mirror setups were discussed by Raffel and Heineck [93]. The easiest choice is to place the mirror axis collinear to the rotor axis, as applied by Overmeyer *et al* [94]. The image now follows the rotor blade if the mirror frequency, f_{mirror}, is half the rotor frequency, f_{rotor}. An off–axis configuration as shown in figure 4 can be useful when the mirror–camera–assembly may not obstruct the rotor shaft and the rotor inflow or outflow.

The infrared images are derotated over the entire blade span if the mirror axis intersects the rotor axis at the hub including an angle β, and the frequencies of mirror and rotor are related by:

$$f_{\text{mirror}} = \frac{1}{2\cos\beta} f_{\text{rotor}}\,, \tag{2}$$

which is a generalization of the on–axis case ($\beta = 0$). The chosen β should not be too large in order to minimize the image distortion due to an oblique viewing angle. Additionally, the periodicity between mirror and rotor must be considered. For example, $\beta = \arccos\left(\frac{3}{4}\right) \approx 41.4°$ results in $f_{\text{rotor}}/f_{\text{mirror}} = \frac{3}{2}$. This means that repetitive images of the blade

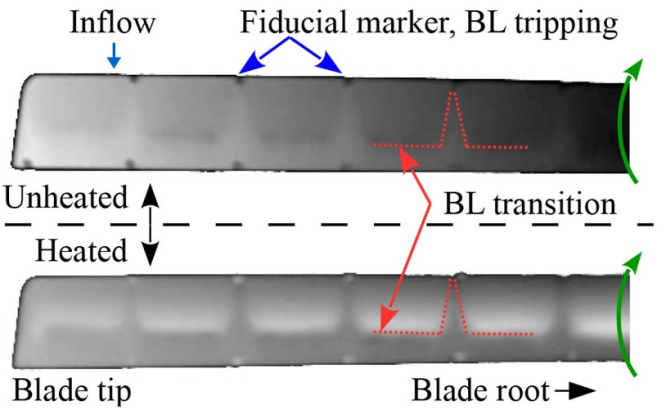

Figure 5. Mirror–derotated images of a rotor blade, adapted from Heineck *et al* [95].

at the same azimuth angle and with the same viewing geometry can be taken every third revolution of the rotor corresponding to every second revolution of the mirror. This choice is a good compromise between the different requirements, and was for example chosen by Weiss *et al* [63].

Heineck *et al* [95] applied IRT and mirror–based derotation to the lower side of a two–bladed rotor with a radius of $R = 0.9$ m, spinning at $f = 15$ Hz in the hover chamber at NASA Ames. The large duration of image exposure, 4.5 ms, covered an azimuthal blade motion of $\Delta\Psi = 24^{\circ}$, but the rotating mirror facilitated sharp infrared images, see figure 5. The blade was radiation–heated by a 1 kW–lamp in the lower image. Hence, the turbulent BL in the rear section of the blade is colder due to the stronger heat convection, and it appears in darker coloring. Fiducial markers used for image registration were placed in regular intervals near the leading edge, resulting in turbulent wedges. The interpretation of the infrared images is identical to static airfoil tests since the aerodynamics is steady in the rotating frame. The upper image is without heating. The transition–related coloring is inverted in comparison to the lower image, since the blade was slightly colder than the heating–up environment, but the pattern has a much lower contrast.

This basic setup was further improved in subsequent measurement campaigns, but rotating mirrors were partly omitted, since newer camera generations offered an improved signal–to–noise ratio at small exposure times. It is noted that measurements of unsteady aerodynamics still benefit from mirror derotation, as shown in the next chapter. Setups with two IR cameras examining both upper and lower blade surfaces were applied by Richter *et al* [85] during ground tests of a prototype full–scale helicopter rotor, and Overmeyer and Martin [83] on a Mach–scaled model helicopter rotor.

Richter and Schülein [82] measured the BL transition on both large–scale model rotors operated on whirl towers, and full–scale helicopter rotors during ground–run and hovering test cases. The infrared camera was mounted obliquely above the rotor plane viewing the blade's upper surface, see figure 6. The image exposure time of down to 20 μs was small enough to avoid motion blur while ensuring a sufficient signal–to–noise ratio to acquire the steady BL transition position. A large number of turbulent wedges is noted due to contamination or surface defects at the leading edge.

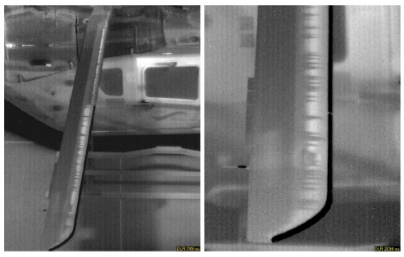

Figure 6. Infrared images of a ground–run test of an Airbus EC135 rotor at 75% of the nominal rotor frequency, Richter and Schülein [82].

4. Unsteady measurements and differential infrared thermography (DIT)

4.1. Principle, pitching airfoil measurements, and optimization

The effects of unsteady inflow conditions on infrared BL transition measurements of a wetted surface can be divided into three categories:

(i) Inviscid aerodynamics govern the time–dependency between the inflow conditions and the surface pressure distribution. For example considering pitch–oscillating airfoils, Theodorsen's theory [96] predicts a hysteresis between the pitch angle and the lift force due to differential velocities induced by shed vorticity in the wake.
(ii) Viscous effects may introduce an additional hysteresis between an airfoil's pressure distribution and the boundary layer's transition position. This effect was shown by Richter *et al* [45] for a pitching airfoil, and confirmed by Gardner *et al* [61].
(iii) The thermal responsiveness, comprising the thermal diffusivity and the specific heat, connects the boundary layer's instantaneous convective heat transfer with the surface temperature as acquired by an infrared camera.

The 'true' aerodynamic transition position only includes effects (i) and (ii), whereas effect (iii) is an error which must be eliminated or reduced by the infrared measurement technique.

When the aerodynamic unsteadiness is sufficiently slower than the thermal responsiveness, steady–state evaluation methods can still be applied. This was shown by Szewczyk *et al* [97], observing the BL transition on a glider wing during a stall–and–recovery maneuver lasting about eight seconds. Simon *et al* [81] discuss the frequency response of infrared transition measurements for several surface materials and heat sources, with response times in the range of several seconds to minutes.

A possible evaluation strategy to overcome thermal hysteresis effects (iii) is differential infrared thermography (DIT), which was proposed by Raffel and Merz [98] and Raffel

et al [99]. The DIT principle is introduced in figure 7, with a more detailed description following in the next sections. The infrared images, left and center, were taken successively during the pitch up–motion of a rotor blade. The aerodynamic–related features are gradual variations of the infrared intensity in chordwise direction, and a prominent turbulent wedge caused by a transition dot. The differential image in figure 7, right, clearly reveals the transition moving forward between both time instants, as seen by a dark band representing decreasing temperatures due to increased cooling. The spanwise variation of the transition is due to three–dimensional effects close to the blade tip.

The difference between steady and unsteady infrared measurements can be seen in figure 8. Figure 8(a), top, shows the chordwise infrared signal of an airfoil's quasi two–dimensional upper surface at static pitch angles, α, of 4.0° and 4.5°. The airfoil was radiation–heated so that the surface temperature, T_W, was slightly above flow temperature. The transition region is located at about $0.25 < x/c < 0.35$, where the surface temperature strongly decreases due to an increasing convective heat transfer. The steepest gradient dT/dx represents 50% intermittence [80].

Subtracting both static temperature distributions results in the differential signal ΔT shown in figure 8(a), bottom. The transition moves forward with increasing α, creating a negative peak at $x_{tr} \approx 0.28$ which can be attributed to 50% intermittence at the mean pitch of $(4.0^\circ + 4.5^\circ)/2 = 4.25^\circ$. Interpreting ΔT is unambiguous, since secondary effects related to uneven heating, to the external flow, or to inhomogeneities in the airfoil's material composition are canceled out. However, it was observed that reflections from the environment of the model must be carefully avoided, since the reflection's position on the model surface may shift during pitch angle variations, creating apparent and erroneous differential signals. Reflections can be prevented by a careful selection of the camera position and by using anti–reflective background material such as cloth curtains.

Infrared measurements at the same pitch angles but taken during a sinusoidal pitch motion are shown in figure 8(b). The thermal inertia of the model's CFRP surface is not negligible compared to the pitch frequency of 2 Hz. Hence, the distributions at $\alpha = 4.0^\circ$ and $\alpha = 4.5^\circ$ are very similar, and the steepest temperature gradient does no longer coincide with the instantaneous transition position. A similar observation is reported by Ikami *et al* [100] using temperature sensitive paint on a pitching airfoil. However, the peak of the differential signal ΔT is still a valid indicator for x_{tr}, even though the peak level is about five times smaller compared to the static measurement. Since the unsteady measurements were taken during the pitch upstroke, the transition position of $x_{tr} \approx 0.295$ is delayed in downstream direction due to hysteresis in comparison to the static value of $x_{tr} \approx 0.28$. It is noted that early DIT publications [99] proposed to not only interpret the DIT peak position but also the width of the peak, connecting the peak's base points to the start and end of the intermittency region. However, it is difficult to identify the base points in the presence of random measurement noise, and aerothermal simulations of pitching airfoils [101] later disproved the concept.

Hoesslin *et al* [102] proposed a concept similar to DIT with a view to turbomachinery applications. In their case, the surface temperature's decline rate after an impulsive flash is measured using high–repetition rate infrared images, which also visualizes the differing heat convection before and after BL transition. The concept should also enable short–term measurements, but so far, only steady airfoil results were published.

The basic principle of DIT was validated and refined in several measurement campaigns for quasi two–dimensional and pitching airfoils. Richter *et al* [46] compared DIT to hot–film data and to the σC_p–method [103] based on fast–response surface pressure transducers. The results cover the DSA-9A helicopter airfoil tested in the Transonic Wind Tunnel Göttingen, see figure 9(a), at $M = 0.3, \mathrm{Re} = 1.8 \cdot 10^6$ and different pitch frequencies up to 8.8 Hz. The infrared camera was a FLIR SC 7750-L LWIR MCT, sensitive in the spectral range of $8.0 - 9.4$ μm, and combined with a 50 mm focal length–lens. The native sensor size was cropped to 640×310 px, enabling an acquisition frequency of 190 Hz at an integration time of 100 μs. Images of the model's untreated CFRP surface were taken through a germanium window in the tunnel's side wall, see figure 9(b). The hot–film sensors are visible as bright spots and can be used for image registration, hence, no fiducial markers were needed. The model was heated with a 2 kW–spotlight mounted outside of the opposite side wall, and differential images of subsequent time steps were calculated. The DIT signal was averaged in spanwise direction, and the peaks were detected similar to figure 8(b).

Figure 9(c) shows the DIT transition data (green dots) as a function of the phase t/T for a sinusoidal pitch motion (dashed black line) taken during multiple pitch cycles. Each data point represents the location x_{tr} of a differential peak, with the peak being either positive or negative depending on whether the transition moves forward or backward. During motion reversal, see the gray areas in figure 9(c), the DIT results are unreliable due to a diminishing signal strength. This problem will treated in the next sections in more detail. Post–processing can be applied to remove outlier and to calculate the phase–averaged transition location. The three experimental methods yield similar results, see figure 9(d), with deviations below 10% of the chord length for this setup. The split between up– and downstroke due to hysteresis effects is largest for DIT, which is a result of the additional measurement lag (iii) due to the surface's thermal responsiveness. The other methods are supposed to cover only the 'true' aerodynamics (i) and (ii).

Wolf *et al* [80] revisited the sinusoidally pitching airfoil model of Richter *et al* [46] in the low–speed '1-meter' wind tunnel at DLR Göttingen, using the same MCT infrared camera and a similar radiation heating with a flux rate in the range of $500 - 1500$ W/m^2 over the suction surface. The inflow Mach and Reynolds numbers were lowered to $M = 0.14$ and $\mathrm{Re} = 1 \cdot 10^6$, increasing the BL's laminar length at a given lift coefficient. The low–speed tunnel enabled cost–effective parameter studies and optimizations of the DIT method. A sketch the setup is in figure 10, which can be taken as a blueprint for similar pitching–airfoil studies [59, 98, 99].

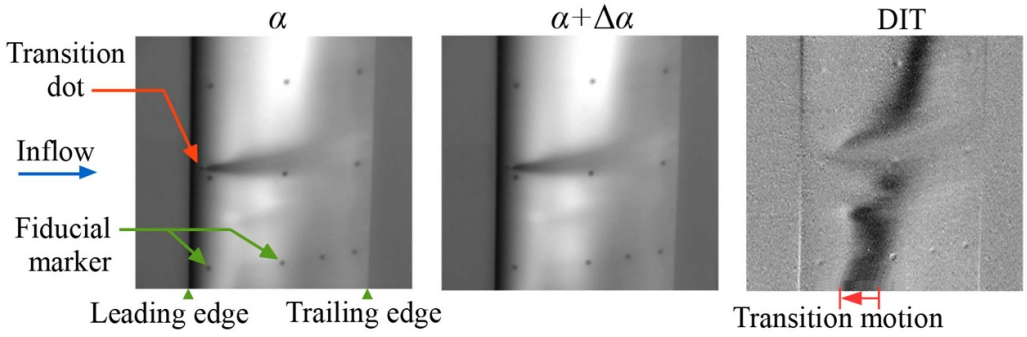

Figure 7. DIT principle, adapted from Raffel *et al* [99].

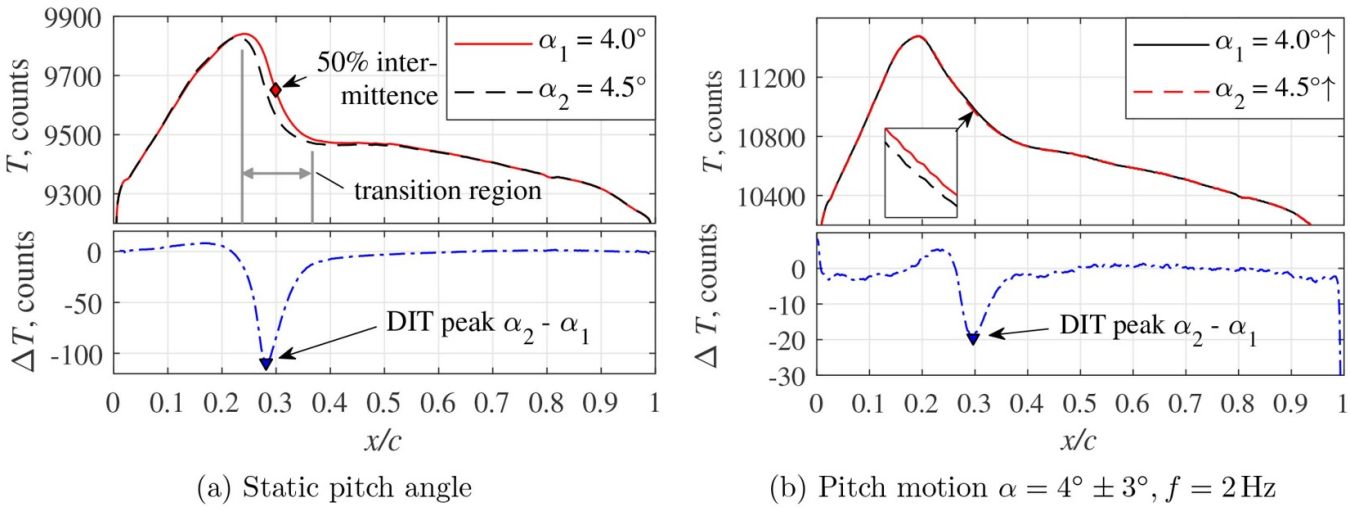

(a) Static pitch angle (b) Pitch motion $\alpha = 4° \pm 3°, f = 2\,\mathrm{Hz}$

Figure 8. Infrared measurements on the DSA-9A helicopter airfoil, $U_\infty = 50\ \mathrm{ms}^{-1}$, data from Wolf *et al* [80].

The main focus of Wolf *et al*'s investigation was set on the influence of the separation distance between two infrared images to be subtracted, which can be expressed as a time difference Δt, or, assuming a periodic pitching motion with frequency f, as a phase difference Δtf. It was shown that it is favorable to detune the acquisition frequency of the infrared camera from the aerodynamic periodicity f with its multiples. Now combining the infrared images of a large number of acquired pitch cycles provides a high resolution of the phase angle, and allows to optimize the phase difference Δtf. In this example, a camera frequency of 99.98 Hz yields a phase resolution of $\Delta tf = 2 \cdot 10^{-4}$. Since the transition–related peaks of ΔT are usually well below 1 K, this approach requires removing the long–term temperature drift, which even in a laboratory environment cannot be avoided, and which may vary with the spatial coordinates due to the model's internal structure or inhomogeneous heating. This is shown in figure 11, in which the black line is a sample unfiltered DIT signal as a function of the chordwise coordinate. The underlying phase difference is small, $\Delta tf = 0.05$ corresponding to 5% of the pitch period, but both images were taken from different pitch cycles with a wall–clock difference of about 40 s. The red line is the high–pass filtered DIT signal, using a cut–off time twice the length of the pitching period. The transition–related peak at $x/c \approx 0.15$ (green arrow) is visible in both distributions, but it is corrupted and slightly biased by temperature drift in case of the unfiltered signal. In contrast, the filtered signal shows a clear peak in the transition region and is nearly zero elsewhere.

The airfoil's DIT transition analysis for sinusoidal pitch oscillations with an amplitude of 7° and a reduced frequency of $k = \pi fc/U_\infty = 0.075$ ($f = 4$ Hz) is shown in figure 12. The green and blue dots correspond to separations of $\Delta tf = 0.005$ and $\Delta tf = 0.05$, respectively. The smaller separation captures the general motion of the transition well, as seen in figure 12(a) (top). The transition position on the upper surface is close to the leading edge at high pitch angles around $tf = 0.5$ but close to the trailing edge at low pitch angles around $tf = 0$ and $tf = 1$. It is noted that the shape of the transition motion is not sinusoidal, since the relation between α and x_{tr} is not linear and depends on the airfoil shape. However, the random scatter of the small separation Δtf is large since the subtracted infrared images are very close, and the resulting DIT peak values shown in figure 12(b) are barely above the camera's noise level. The ratio between peak values and underlying measurement noise is crucial for the achievable spatial and temporal resolution of the DIT analysis. The random scatter is reduced for large DIT image separation, see figure 12(a) (bottom). This corresponds to an increased peak signal strength as in figure 12(b), with the negative or positive sign of the peak depending on whether the motion is towards the leading or trailing edge.

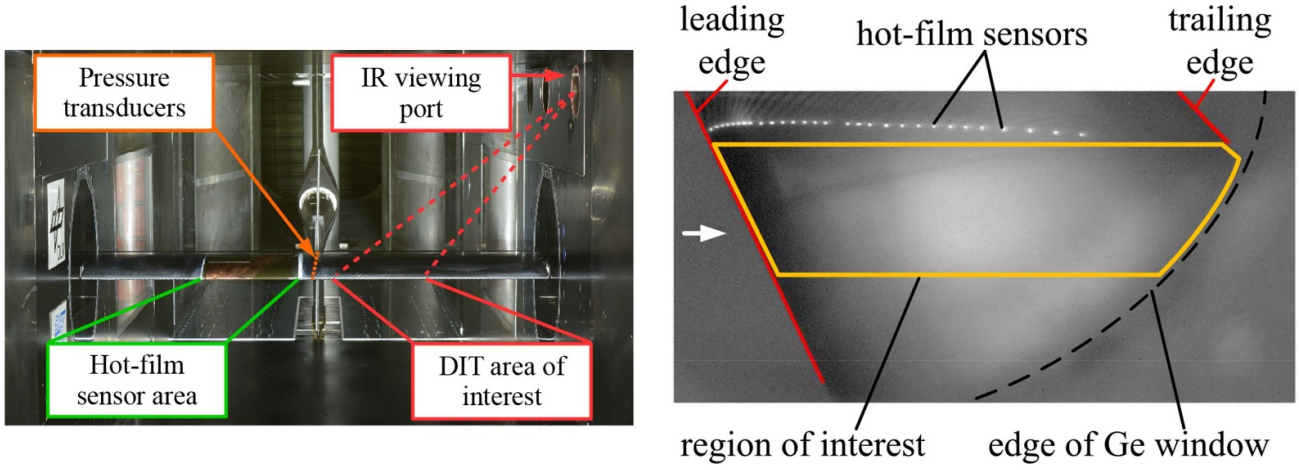

(a) Setup viewed in downstream direction

(b) Sample infrared image

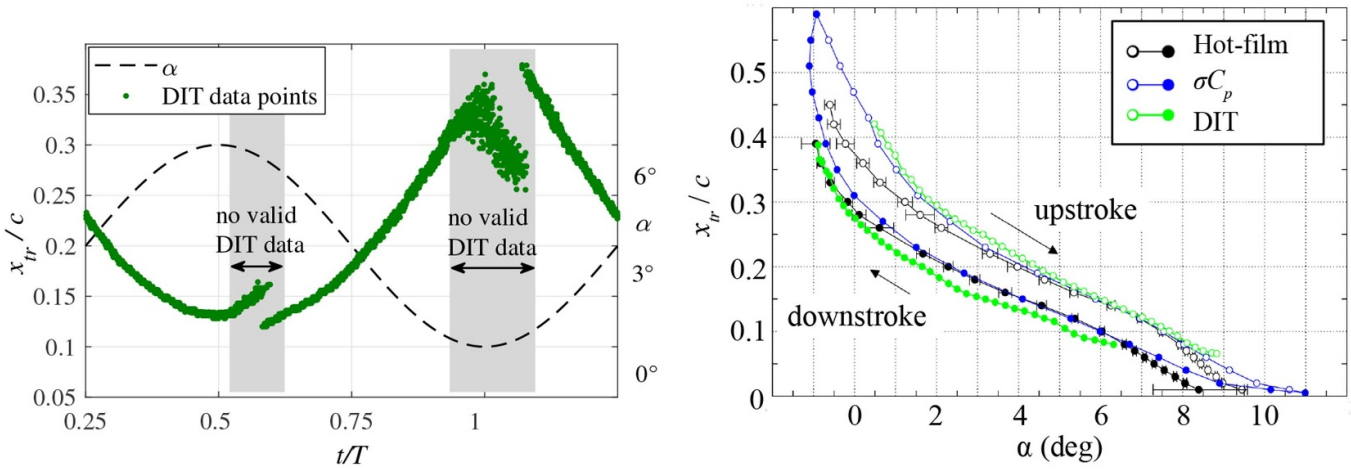

(c) DIT transition points, $f = 4.4\,\mathrm{Hz}$, $\alpha = 3° \pm 3°$

(d) Method comparison, $f = 6.6\,\mathrm{Hz}$, $\alpha = 5° \pm 6°$

Figure 9. Transition measurements on a pitching airfoil using three experimental methods, see Richter *et al* [46].

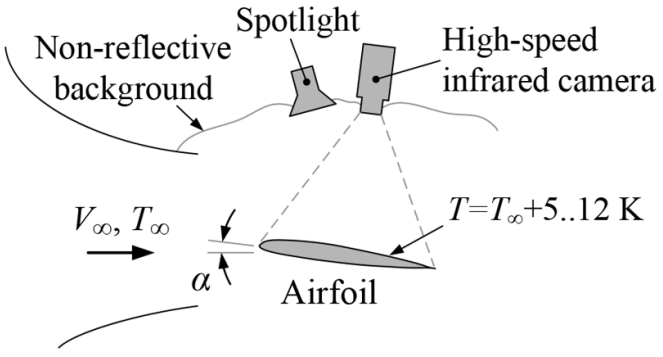

Figure 10. Sketch of a DIT wind–tunnel setup [80].

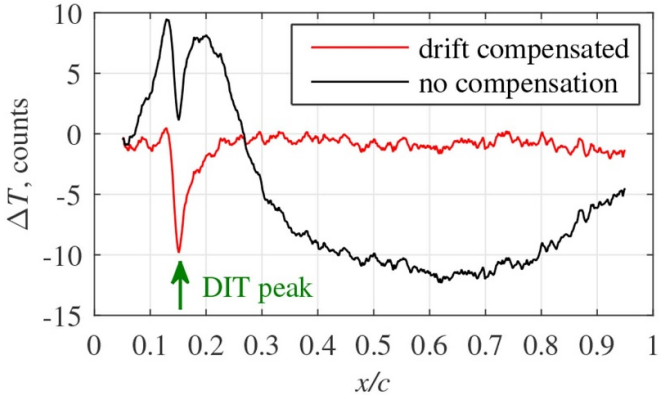

Figure 11. DIT temperature drift correction using a high–pass filter [80].

Despite the large separation, the differential signal diminishes towards the frontmost and backmost positions where the movement of the transition is slower. Particularly at $tf = 0.5$, the same bifurcation as in figure 9(c) is observed. This bifurcation can be attributed to a DIT double–peak structure, see the red detail in figure 12(a) (bottom), with a coexistence of both positive and negative peaks. Assuming that the peak search algorithm detects the maximum peak value regardless of its sign, the results will randomly switch between both states, creating the bifurcation. A detailed analysis in the next section

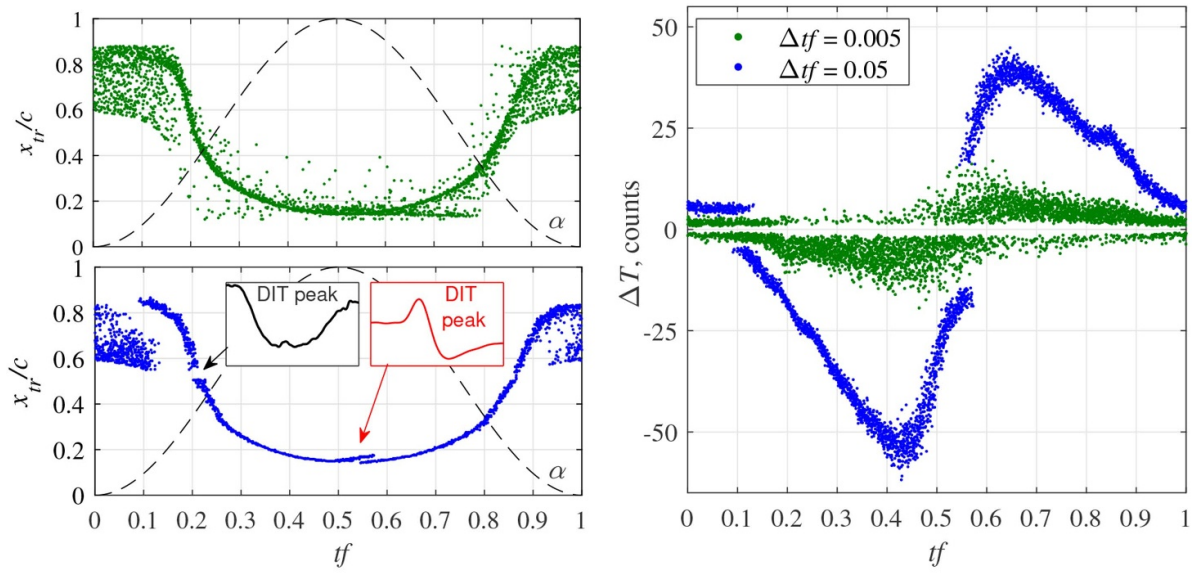

(a) Position of DIT peak, BL transition (b) Value of DIT peak

Figure 12. DIT analysis of a pitching airfoil, suction surface, $k = 0.075$, $\alpha = 4^\circ \pm 7^\circ$, DIT separation $\Delta tf = 0.005$ (green dots) and $\Delta tf = 0.05$ (blue dots), see [80].

will show that the true transition position is in between. At $tf = 0.2$, the large separation of $\Delta tf = 0.05$ produces another gap in the transition data. This can be attributed to a broad negative–negative DIT double–peak structure, see the black detail in figure 12(a) (bottom). At this chordwise position the transition motion is fast and the intermittency regions in both infrared images no longer overlap, hence, the single DIT peak starts to split up into two separate peaks.

This raises the question of the optimal infrared image separation Δtf, with figure 13 showing the influence of Δtf on the parasitic measurement hysteresis (iii). This hysteresis is defined as the pitch difference, $\Delta\alpha$, between the up- and downstroke for a given transition position. The true aerodynamic hysteresis as seen by the σC_p–method was subtracted, so $\Delta\alpha = 0$ means an error–free DIT measurement. The hysteresis depends on multiple factors such as the pitch motion, the airfoil's geometry and surface material, the infrared camera's signal–to-noise ratio, etc. For a variation of the transition position, figure 13(a), and a variation of the reduced pitch frequency k, figure 13(b), three universal effects can be identified: In region **a)** the measurement hysteresis decreases with decreasing phase separation, since the subtracted infrared signals successively converge on the instantaneous state of the flow. The minimum measurement hysteresis, limited by the thermal responsiveness of the airfoil's surface, is reached in region **b)**. A further reduction of the separation in region **c)** yields an increasing scatter and measurement uncertainty since the diminishing temperature difference between to images approach the camera's noise limit.

Gardner *et al* [101] conducted a 2D URANS simulation of Richter *et al*'s [46] and Wolf *et al*'s [80] experiment, including aerodynamic hysteresis effects. The predicted instantaneous skin friction coefficient C_f was coupled to a 1D simulation of the unsteady heat transfer in the airfoil's wall–normal direction, allowing the evaluation of synthetic temperature distributions and derived DIT results. The study generally confirmed the validity of the DIT method, but also provided new insight into problems connected to the thermal responsiveness. Figure 14 shows the predicted chordwise differential temperature distributions, ΔT, before and after the reversal of the pitch motion at the minimum pitch angle, corresponding to a phase of $ft = 0$.

The sign of the peak expectedly changes from positive to negative. When the motion of the transition stops in its most rearward position at about $x/c = 0.55$, the ΔT–signal should be zero for a surface material with infinite responsiveness and no thermal lag. When introducing a finite thermal responsiveness, both positive and negative peaks are coexistent, which is particularly visible for the dark blue line at $ft = 0.021$. This simulation result has a strong qualitative resemblance to the experimental differential signal shown in the red detail in figure 12(a) (bottom). The 'double–peak'–structure yields systematic errors, which explain the bifurcation of the DIT data points observed in the gray areas of figures 9(c) and 12(a) (bottom). The true aerodynamic transition positions marked by dots in figure 14 are between the positive and negative peaks, and they do not coincide with the detected 'phantom' peaks marked by the dashed black locus curve.

Gardner *et al* [101] further investigated the effects of different surface materials, assuming that the DIT measurements benefit from both a low thermal diffusivity and a low specific heat. The results shown in figure 15 are referenced to the epoxy matrix material used for the CFRP model in Richter *et al* [46]. Even the best insulators, expanded polystyrene and cork, offer only moderate reductions in terms of DIT thermal delay representing the hysteresis (top graph).

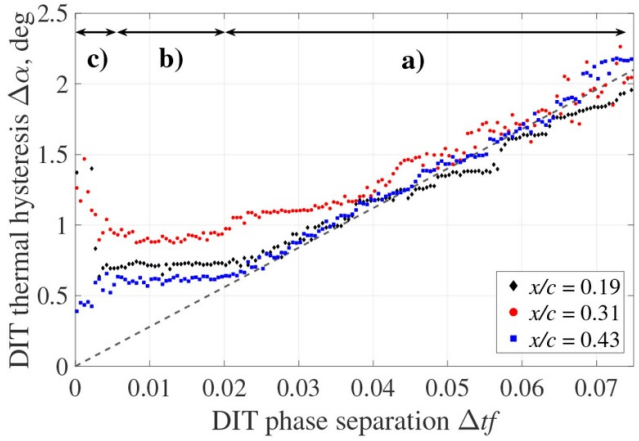

(a) Transition at different x/c, reduced frequency $k = 0.075$, $\alpha = 4° \pm 7°$

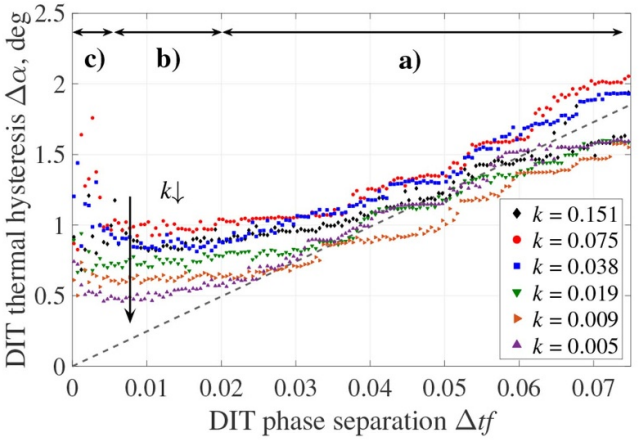

(b) Different reduced frequencies k, transition at $x/c = 0.31$, $\alpha = 4° \pm 6°$

Figure 13. Thermal hysteresis $\Delta\alpha$ as a function of the DIT image separation Δtf, see [80].

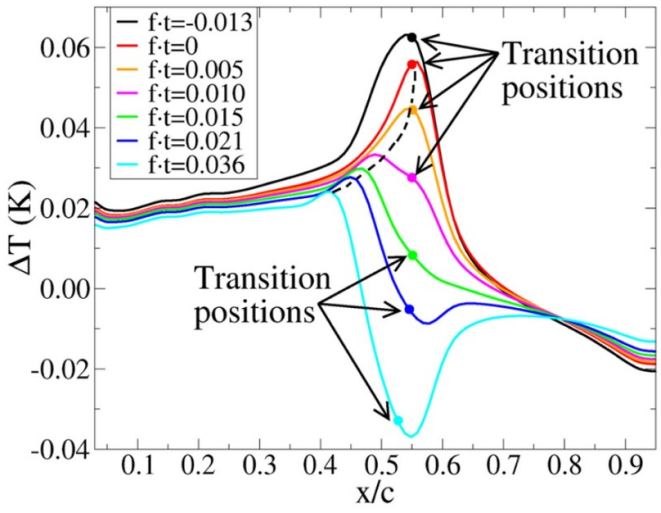

Figure 14. Synthetic DIT results at the reversal of the pitch motion, $f = 6.6$ Hz, $\alpha = 5° \pm 6°$, see [101].

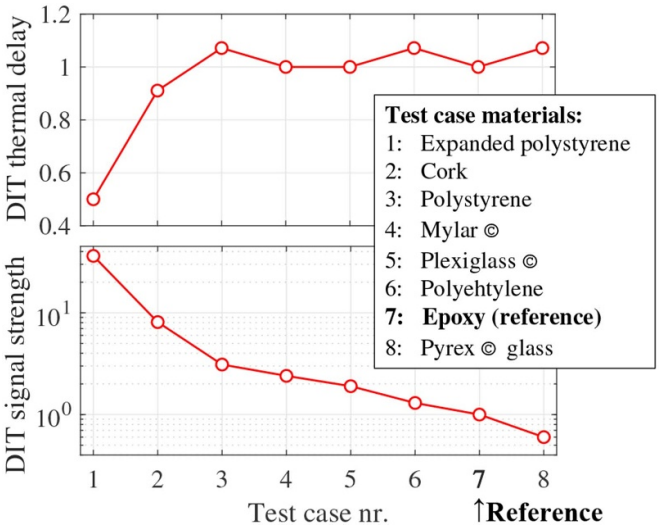

Figure 15. Comparison of surface materials, relative DIT thermal delay (top) and signal strength (bottom), adapted from Gardner *et al* [101].

On the other hand, the peak strength of ΔT can be significantly increased by a factor of 10 and more (bottom graph). This result motivates the application of surface coatings, as it was also shown that the unsteady temperature variations are restricted to a very thin surface layer with a thickness below 0.5 mm. On the other hand, the coating's application, its mechanical strength, and its surface roughness have to be considered.

Based on these observations and using the same experimental setup [80] Mertens *et al* [53, 104] proposed that the image separation should be optimized with respect to a quality indicator which accounts for data scattering. This approach is particularly suitable for sinusoidal pitch motions, in which the speed of the transition motion and the corresponding differential infrared signal strongly varies over the pitch cycle.

Mertens *et al* [53] also proposed local infrared thermography (LIT) as a variant of DIT which adds further insight to the thermal responsiveness. A high phase resolution of the infrared images allows the analysis of the temperature T at a given position x/c over the entire pitch cycle. This is shown in figure 16, left, in which the temperature signal at $x/c = 0.31$ was low–pass filtered with sliding average window sized $\Delta tf = 0.02$ (2% of the pitch cycle) to reduce noise. The convective cooling effect of the turbulent BL is clearly seen by means of a decreasing temperature between about $tf = 0.24$ and $tf = 0.78$. The transition passes slightly after the temperature peaks, see the square symbols in figure 16 (left), but before the peaks of the numerically derived temperature gradient $dT/d(ft)$, see the circular symbols in figure 16 (right). It is noted that analyzing this local temperature gradient is equivalent to the DIT approach with a very small image separation Δtf. LIT reduces the data scatter noted in the DIT results of

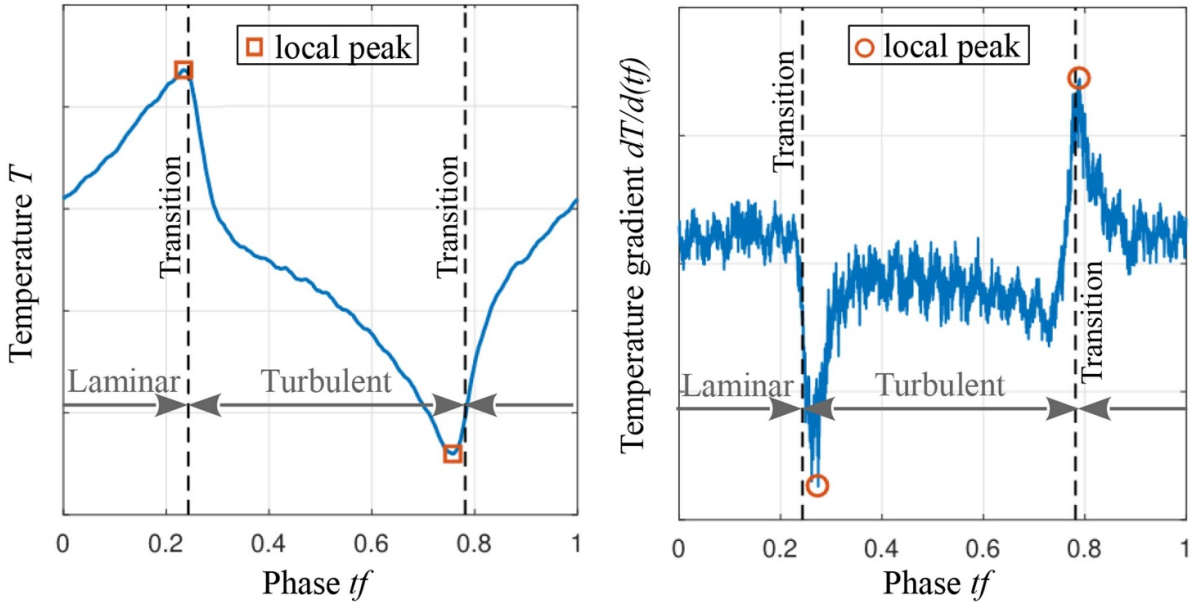

Figure 16. LIT, local temperature (left) and local temperature gradient (right) at $x/c = 0.31$ for $k = 0.075$ and $\alpha = 4^\circ \pm 6^\circ$ [53].

figure 13 for $\Delta tf \to 0$ by applying the aforementioned sliding window filter.

Using optimized evaluation procedures and infrared data with a good signal–to–noise ratio, it is possible to extend the differential analysis to produce two–dimensional results down to the resolution of a single pixel [53, 104]. This particularly avoids taking the spanwise average of airfoils as in [46, 80]. Figure 17 shows the two–dimensional LIT analysis during the upstroke of a sinusoidal pitch motion, considering the airfoil's suction side with the flow from left to right. The detected transition area is marked in blue color and superimposed onto the original infrared image data. For an increasing pitch angle, left to right, the transition moves towards the leading edge. The smallest pitch angle, figure 17 (left), shows three–dimensional effects by means of a slightly tilted BL transition line interrupted by three transition wedges marked by green triangles. The top and bottom wedges result from an increased surface roughness due to the painted fiducial markers appearing as black dots in the images. The central wedge is caused by surface pressure taps which are not seen by the infrared camera. In this chordwise area small perturbations have a strong influence on the transition position due to the flat pressure distribution. Towards the leading edge, the transition is mainly caused by the strong pressure gradient dp/dx downstream of the suction peak. Hence, the influence of surface defects is smaller, and the transition line becomes more two–dimensional as in figure 17 (right).

4.2. Rotor measurements

Measurements of unsteady BL transition locations on rotating or fast–moving aerodynamic surfaces is one of the most challenging tasks for infrared thermography, since most of the difficulties described in the earlier sections add up.

The first successful application of DIT to a subscale rotor was demonstrated at the rotor test stand Göttingen (RTG) by Raffel *et al* [99], providing data on moving BL transition for unsteady conditions complementing earlier steady–state test cases [74, 105]. The RTG, see figure 18, enables an azimuth–varying blade pitch through a swashplate similar to helicopters, but it has a horizontal axis and does not simulate edge–wise inflow as in helicopter forward flight. The RTG is optimized for the synchronized application of blade–mounted sensors, such as pressure transducers, and external optical camera systems.

A similar test with an improved setup and rotor frequencies up to 23.6 Hz was conducted by Weiss *et al* [63]. The application of a high–speed infrared camera and a rotating mirror allowed the acquisition of both DIT measurement images to be subtracted during a single rotor revolution with a constant azimuthal separation of $\Delta\Psi = 18^\circ$, corresponding to a phase separation of $\Delta tf = 0.05$ and an image frequency of 472 Hz. The camera was a FLIR X8500sc SLS LWIR, which is sensitive in the spectral range of $7.5 - 12$ μm. The image integration time was set to 57 μs, which is lower in comparison to the MCT camera used in [80, 99] due to a superior signal–to–noise ratio (NETD: 20 mK versus 35 mK). The spatial resolution was 2 mm/px using a 50 mm focal length–lens. The radiative heat flux provided by halogen lamps was about $400 - 500$ W/m^2, which is on a similar level as in [80].

DIT transition results for the suction side of the rotor blade and at a radial station of $r/R = 0.8$ are shown as black dots in figure 19. The unsteady inflow conditions were produced by a cyclic swashplate setting with a pitch amplitude of about 6°, and the data is similar to pitching–airfoil data shown in the preceding section. A comparison to steady–state IRT results at the corresponding constant pitch angles, marked by blue squares

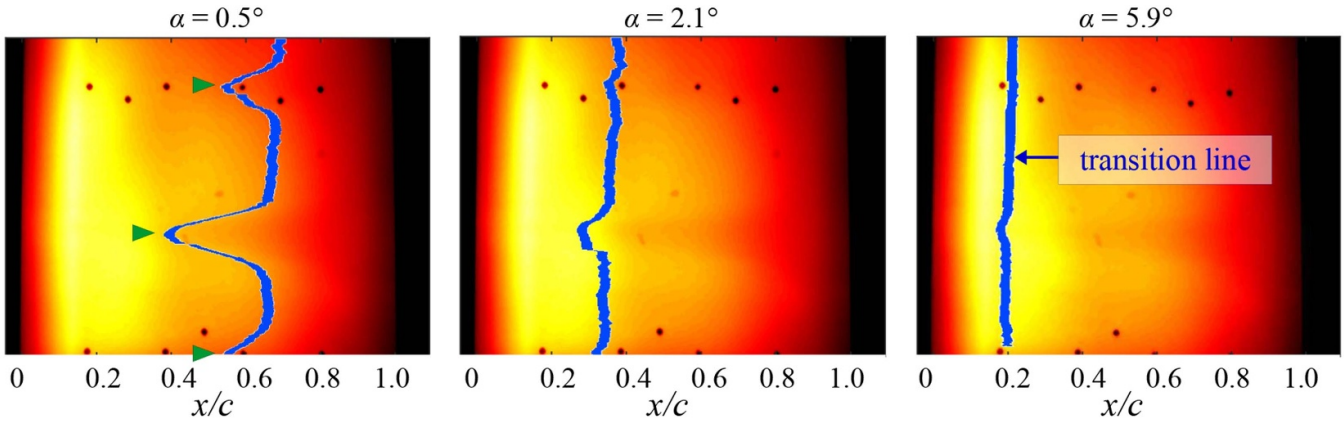

Figure 17. LIT transition measurement in a 2D–domain, pitching airfoil (upstroke), suction surface, $k = 0.075$, $\alpha = 4^\circ \pm 6^\circ$ [53].

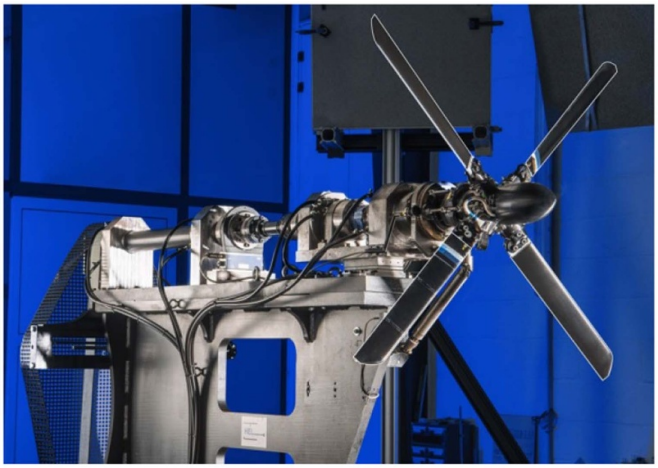

Figure 18. Rotor test stand at DLR Göttingen (RTG).

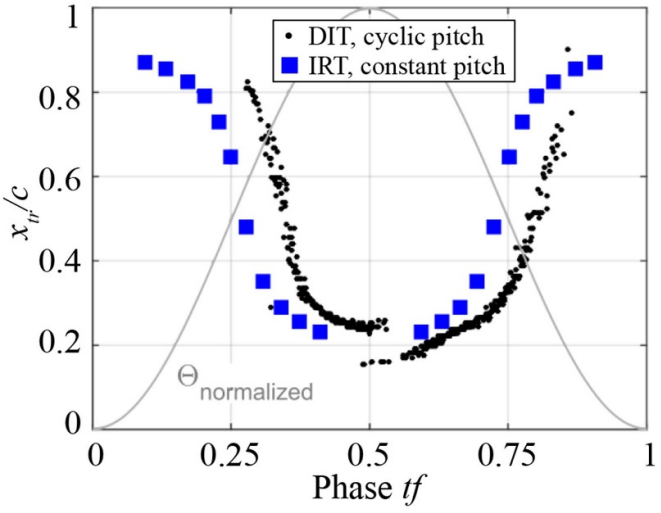

Figure 19. RTG transition position at $r/R = 0.8$, IRT results for static pitch angles, DIT results for cyclic pitch input, $f = 23.6$ Hz, pitch amplitude $\hat{\Theta} = 6^\circ$ [63].

in figure 19, reveals the aerodynamic hysteresis by means of a shift towards larger phases *tf*, that is, towards the right side.

The combined results at the radial stations between $r/R = 0.4$ and 1.0 can be visualized in a polar coordinates, forming the transition map shown in figure 20 (left). The experimental data is compared to a numerical DLR TAU simulation of the experiment in figure 20, right. The simulation was set up based on the best practices described by Kaufmann *et al* [106], and the overall agreement of the BL transition position x_{tr} is very good. The minimum and maximum pitch angles are at the top and bottom of the rotor plane maps, respectively. Note that the transition pattern, with light colors indicating x_{tr} close to the trailing edge and dark colors indicating x_{tr} close to the leading edge, is roughly symmetric but slightly rotated in counterclockwise direction representing aerodynamic hysteresis effects.

The model–scale measurements provide a rough estimate for the operating range of DIT using current infrared camera technology. Figure 21 shows the DIT thermal hysteresis (iii) as an excess pitch $\Delta\Theta$ over the true aerodynamic hysteresis, corresponding to the definition used in figure 13. The data of references [46, 63, 80] is plotted as a function of the airfoil's or blade's pitch rate. For decreasing pitch rates below about 15°/s, see the detail in the right figure, the thermal hysteresis monotonically decreases towards zero, representing an error–free transition measurement for static conditions. For larger and technically relevant pitch rates the thermal hysteresis is bounded by about 1° to 1.5°, neglecting a single outlier at 2.3° [63]. Nevertheless, the DIT principle was demonstrated even for very high pitch rates up to almost 900°/s. It is noted that the stated thermal pitch hysteresis $\Delta\Theta$ cannot be generally converted into a bias of the detected transition position, since the corresponding transition motion highly depends on the airfoil shape.

Overmeyer *et al* [94] conducted the first BL transition measurement of a trimmed rotor in forward flight conditions, applying DIT to the lower side of the three–bladed NASA PSP model rotor with a radius of 1.7 m. The rotor was operated in the Langley 14×22–Foot Subsonic Tunnel at $f = 18.2$ Hz and advance ratios up to $\mu = 0.38$. DIT images were calculated by subtracting dewarped infrared images with an azimuthal spacing of about 23°. The interpretation of the results is different compared to the preceding sections due to the

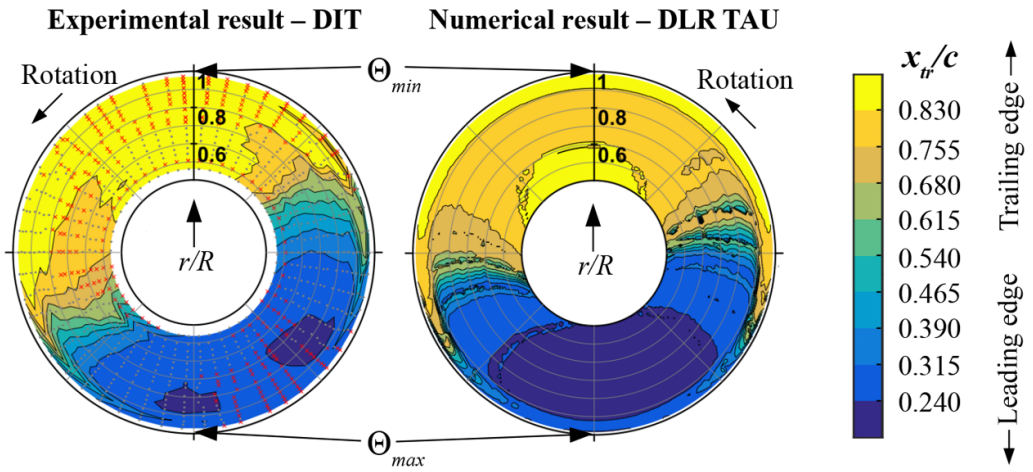

Figure 20. RTG transition, DIT results for cyclic pitch input, $f = 23.6$ Hz, pitch amplitude $\hat{\Theta} = 6^{\circ}$, data from Weiss *et al* [63].

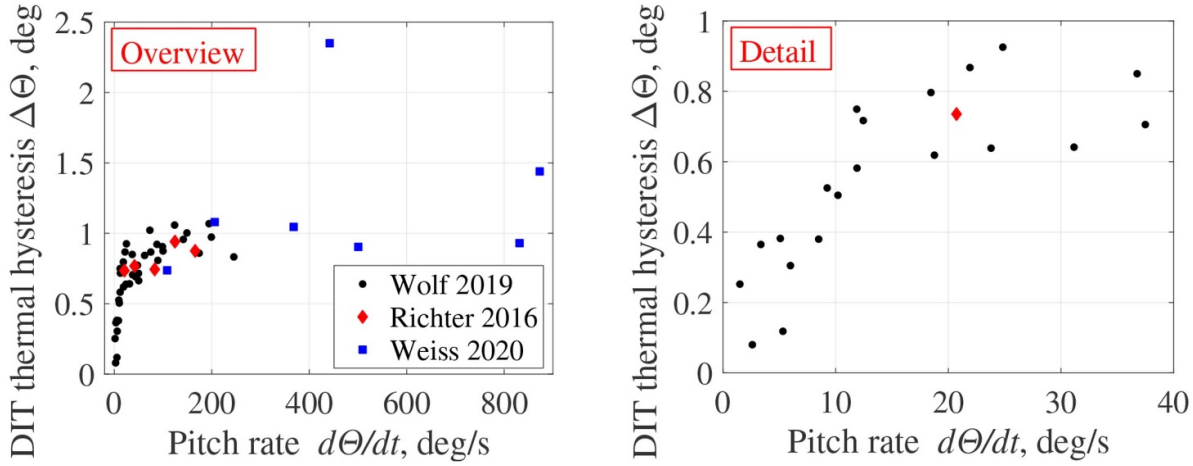

Figure 21. Thermal hysteresis $\Delta\Theta$ as function of the pitch rate $d\Theta/dt$, data from Richter *et al* [46], Wolf *et al* [80], and Weiss *et al* [63], overview (left) and detail (right).

sinusoidal variation of the blade's inflow velocity and, therefore, the stagnation temperature as a function of the azimuth angle. On the advancing side of the rotor plane, see figure 22(a), the external flow is warmer than the blade, and the turbulent areas heat up faster than the laminar areas. The BL is almost fully turbulent in the inboard sections of the blade, whereas large laminar pockets at the tip are interrupted by turbulent wedges resulting from artificial transition dots. On the retreating side, see figure 22(b), the blade is cooled by the flow, and this effect is amplified in turbulent areas. The BL on the lower surface is fully laminar, again except for the forced turbulent wedges near the blade tip. Since both laminar and turbulent regions appear as coherent areas with nearly uniform temperature changes, the differential images resemble individual infrared images for steady–state flow conditions. In agreement with the aerothermal simulations and experimental findings by Gardner *et al* [107], the transition can therefore be detected by means of the first edge (gradient) seen from the trailing edge, which avoids differential signals due to suction peak–related changes close to the leading edge. This is a deviation from DIT with continuous blade heating, in which only the moving laminar/turbulent interface appears as a differential peak signal. For Overmeyer *et al*'s experiment an additional constant blade heating was disregarded, since a superposition with the inevitable periodic temperature change partly led to a decreased signal–to–noise ratio of the DIT images.

Based on these findings Gardner *et al* [107] conducted in–flight infrared measurements of an Airbus EC 135 helicopter at a forward flight speed of 80 kn, taking images of the rotor's upper surface from a second chase helicopter as seen in figure 23. The distance between both helicopters was $50 - 100$ m limited by safety considerations. The same high–speed SLS camera as in [63] was used. The frame rate was set to 294 Hz, corresponding to a phase difference of $\Delta tf = 0.022$, or an image–to–image blade motion of $\Delta\Psi = 8^{\circ}$. The infrared images were acquired with a cropped sensor size of 768×800 px and an integration time of 50 μs, which sufficiently suppresses motion blur even without a rotating mirror. A telescopic lens with a focal length of $f = 200$ mm was applied to the camera. The maximum blade pitch rate due to cyclic swashplate inputs was estimated using trim calculations to about 150°/s, which is well within the DIT range

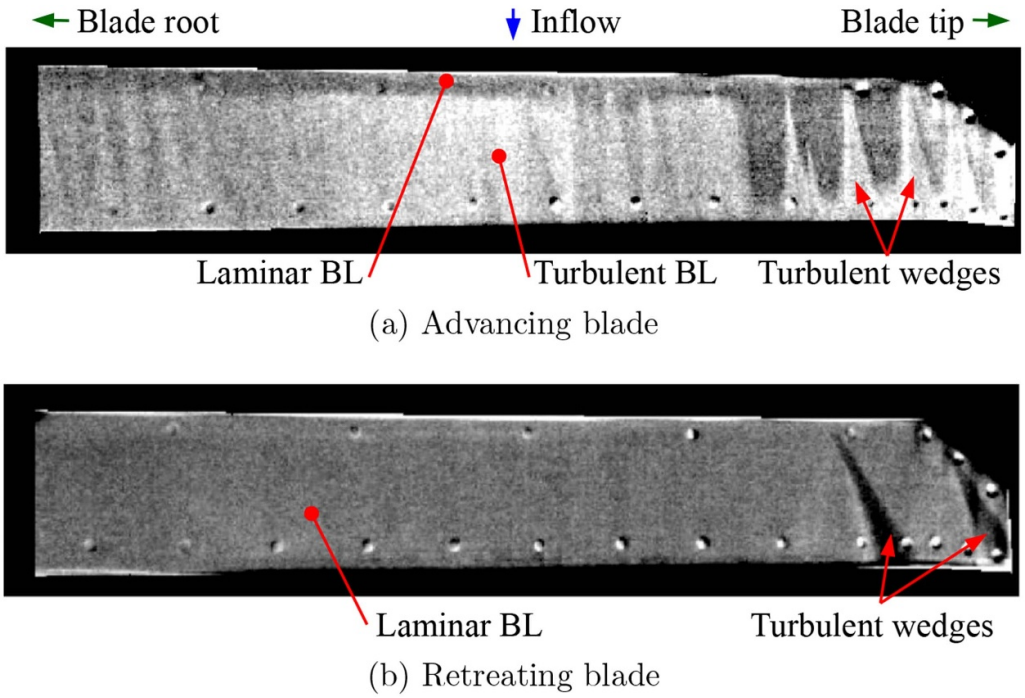

Figure 22. DIT evaluation of a subscale rotor in forward flight conditions, light (dark) colors show increasing (decreasing) temperatures, adapted from Overmeyer *et al* [94]

demonstrated in figure 21. However, no artificial blade heating was available, and the measurements solely relied on the azimuthal variation of the stagnation temperature.

The blade surface temperature increases in radial direction and proportional to Ωr^2, see figure 24 (left), reflecting the average stagnation temperature of the inflow. The variation of the surface temperature over the rotor plane's azimuth angle is small, but by tendency, the blade is heated on the advancing side (azimuth 0° to 180°) and cooled on the retreating side (azimuth 180° to 360°) due to the sinusoidal change of the stagnation temperature. The peak–to–peak difference between local stagnation temperate and average blade temperature is about 20 K in the midspan region, see the black line in figure 24 (right). The corresponding reaction of the instantaneous surface temperature is in the sub–Kelvin regime and phase–delayed due to the limited thermal responsiveness of the blade surface at the rotor frequency of $f = 6.6$ Hz. However, the infrared–measured data (red dots) generally follows the numerical prediction of the surface temperature (green line), but the variations approach the camera's noise limit.

Nevertheless, Gardner *et al* [107] successfully applied DIT, and identified a region between leading edge and about 20% chord which shows a differential signal on the advancing side of the rotor plane. Unfortunately, the DIT result could not be unambiguously connected to BL transition, since this area was also covered by an erosion tape. It was known from hover tests that the step between the tape's trailing edge and the blade surface triggers transition, but the DIT is also affected by the different thermal responses of both surface materials, with both transition and responsiveness effects adding up in differential images. Even though the general DIT principle was demonstrated, future in–flight measurements will benefit from rotor blades with a larger amount of laminar flow over the blade and a better optical resolution of the images, which in this study was limited by the minimum safety distance between both helicopters and the available lens optics for infrared cameras.

4.3. DIT–based stall detection

Some of the experiments in the preceding section showed as a by–product that DIT is also an efficient tool to detect BL separation. Airfoil testing by Gartenberg *et al* [108] already noted that flow separation affects the time–averaged convective heat transfer, with a low convection in laminar separation bubbles due to recirculating flow, but a high convection in fully separated regions due to vortex shedding. This enables an evaluation similar to steady–state IRT, as also shown later by Montelpare and Ricci [109]. The separation detection can now be extended to fast-moving surfaces and short time intervals using modern infrared cameras and the DIT method, which in this case exploits the unsteadiness of the flow separation.

Figure 25(a) shows two differential infrared images of an airfoil's upper surface. Instantaneous images at different times but at the same pitch angle were subtracted. This yields no relevant difference apart from camera noise for attached flow (top) but strong variations for fully separated flow (bottom). Gardner *et al* [59] interpreted this pattern as the footprint of large–scale coherent and three–dimensional flow structures shed within the separated region. Therefore, flow separation can be detected by means of a high standard deviation within the DIT images, either in spatial or temporal direction. The spatial standard deviation, σDIT, within a window close to

Figure 23. EC 135 in–flight infrared image, blade temperatures highlighted in pseudocolors, with an agricultural field in the background (left), Bo105 chase helicopter with hand–held infrared camera seen in the open passenger compartment (right) [107]

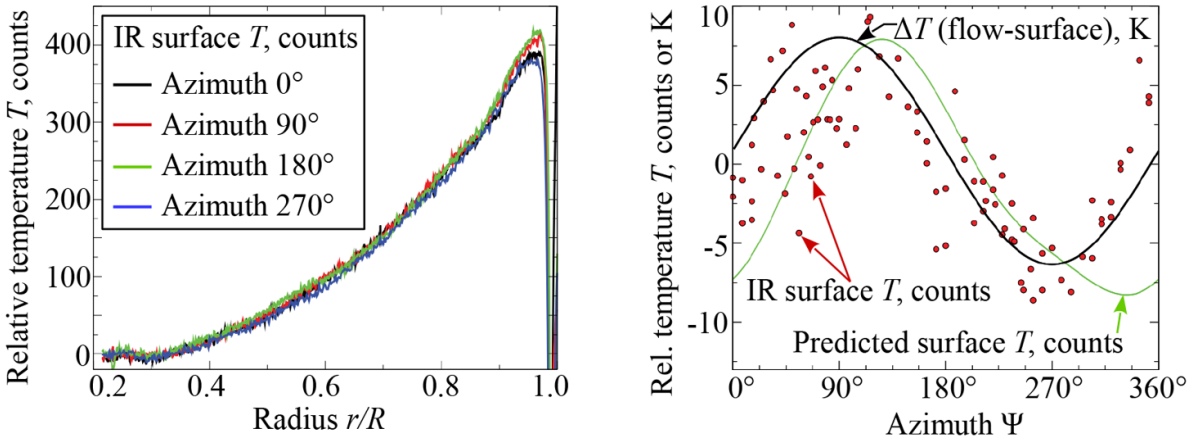

Figure 24. EC 135 blade temperatures, radial distribution (left), azimuthal distribution at $r/R = 0.5$ (right) [107]

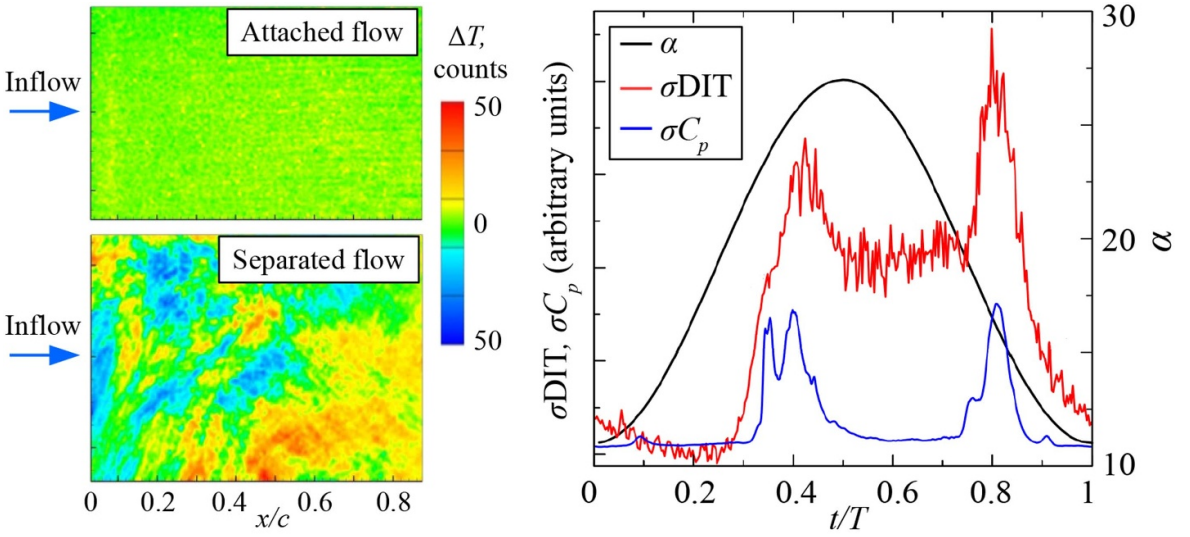

(a) Differential infrared images

(b) Standard deviation σ for DIT and C_p, pitch–oscillating airfoil in dynamic stall conditions

Figure 25. DIT stall detection applied to an airfoil surface, adapted from Gardner *et al* [59]

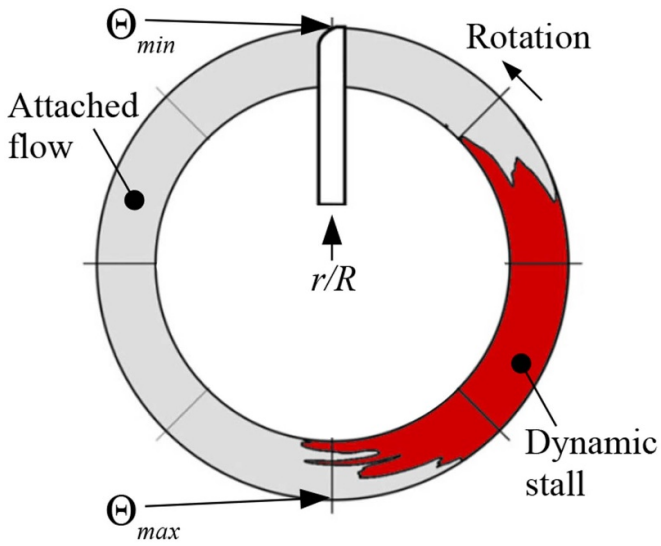

Figure 26. Dynamic stall map for a rotor with cyclic pitch input, $f = 23.6$ Hz, pitch amplitude $\hat{\Theta} = 6°$, data from Raffel *et al* [110]

the leading edge of the airfoil in deep–stall pitch oscillations is shown as red line in figure 25(b). Two distinct DIT peaks at about $t/T = 0.4$ and $t/T = 0.8$ are related to flow separation and flow reattachment, as a comparison to the blue line of the surface pressure–based σC_p–method shows. Apart from both σDIT–peaks there is a low level of thermal unsteadiness during attached conditions and a medium level of unsteadiness during fully separated flow. It is noted that a quantitative relation between σC_p and σDIT is neither meaningful nor required for separation detection, hence, the quantities are shown in arbitrary units, eliminating the need for extensive sensor and camera calibrations.

Raffel *et al* [110] utilized the setup at the rotor test stand Göttingen, see figures 18 and 20, but increased the collective pitch setting so that dynamic stall was initiated during the downstroke motion of the blade. The stall map shown in figure 26 was acquired using the DIT principle and successfully compared to point–wise dynamic pressure transducers.

5. Conlusions

The main conclusions of recent developments in steady and unsteady infrared thermography for boundary layer (BL) transition detection can be summarized as follows:

(i) Infrared thermography (IRT) is an easy–to–use standard technique measuring the spatial distribution of the non–moving laminar–turbulent BL transition. It can be adapted to rotor applications with steady inflow conditions.
(ii) Recent developments in high–speed, short–exposure infrared cameras with photon detectors permit the acquisition of instantaneous unsteady infrared images.
(iii) The interpretation of instantaneous infrared images must consider the thermal responsiveness of the surface material, which is generally non–negligible in aerodynamic applications.
(iv) Differential techniques can be used in standardized image processing methods such as differential infrared thermography (DIT) to overcome or reduce the thermal history effects of the surface.
(v) DIT was applied to several pitching–airfoil tests and rotor tests, showing a good agreement but an additional measurement–related lag in comparison to point–wise fast–response data provided by hot–films or pressure transducers. DIT is also a useful tool for an unambiguous interpretation of steady transition positions.
(vi) The separation distance between the two subtracted infrared images is an important parameter of differential methods. The optimal DIT separation will depend on both aerodynamics and experimental setup. An a–posteriori optimization is often possible under laboratory conditions when carefully choosing the acquisition frequency. For the current studies, a separation of 1% to 2% of the aerodynamic cycle provided good results and can be taken as a rule–of-thumb suggestion.
(vii) Short–exposure infrared images can additionally be used to detect other aerodynamic phenomena such as flow separation.
(viii) Unsteady infrared thermography is a very promising candidate for full–scale measurements, for example on helicopter main rotors or wind turbine blades during operation. First applications showed promising results, but further improvements in both camera technology and rotor blade performance are needed to validate the principle.

Acknowledgment

The authors thank all colleagues involved in the presented studies (in alphabetical order): Miles Barnett, Johannes Braukmann, Christoph Dollinger, Christian Eder, Benjamin Ewers, Uwe Göhmann, Andreas Goerttler, James T. Heineck, Kurt Kaufmann, Markus Krebs, Christoph Mertens, Austin D. Overmeyer, Christoph Merz, Kai Richter, Erich Schülein, Clemens Schwarz, Till Schwermer, Armin Weiss, and the 'Flight Experiments'–team at DLR Braunschweig.

References

[1] Egolf T A, Harigaran N, Narducci R and Reed E 2017 AIAA standardized hover simulation: Hover performance prediction status and outstanding issues *AIAA SciTech Forum* (*Grapevine, TX*) (Reston, VA: AIAA)
[2] Beaumier P and Houdeville R 1995 3D laminar-turbulent boundary layer calculations on helicopter rotors in forward flight: application to drag prediction *21st European Rotorcraft Forum* (*St Petersburg, Russia*)
[3] Beaumier P, Zibi J and Costes M 1997 CFD drag and power prediction for a rotor in hover and forward flight *J. Am. Helicopter Soc.* **42** 327–36
[4] Zografakis G, Barakos G and Johnson M 2008 Transitional modelling for rotorcraft CFD *34th European Rotorcraft Forum* (Liverpool: University of Liverpool)
[5] Coder J G 2017 Overflow Rotor Simulations Using Advanced Turbulence and Transition Modeling *55th AIAA*

Aerospace Sciences Meeting, AIAA SciTech Forum (Grapevine, TX, 09-13 January) (Reston, VA: AIAA)
[6] Heister C C 2018 A method for approximate prediction of laminar–turbulent transition on helicopter rotors *J. Am. Helicopter Soc.* **63** 1–14
[7] Richez F, Nazarians A and Lienard C 2017 Assessment of laminar-turbulent transition modeling methods for the prediction of helicopter rotor performance *43rd European Rotorcraft Forum (Milan)*
[8] Schwarz T and Pahlke K 2012 Generation of an advanced helicopter experimental aerodynamic data base for CFD validation - the European GOAHEAD project *Aerosp. Sci. Technol.* **19** 1–2
[9] Dick E and Kubacki S 2017 Transition models for turbomachinery boundary layer flows: A review *Int. J. Turbomach. Propuls. Power* **2** 4
[10] Nürnberger D and Greza H 2002 Numerical investigation of unsteady transitional flows in turbomachinery components based on a RANS approach *Flow Turbul Combust* **69** 331–53
[11] Liu X and Rodi W 1991 Experiments on transitional boundary layers with wake-induced unsteadiness *J. Fluid Mech.* **231** 229–56
[12] Orth U 1993 Unsteady boundary-layer transition in flow periodically disturbed by wakes *Journal Turbomach.* **115** 707–13
[13] Schobeiri M T, Read K and Lewalle J 2003 Effect of unsteady wake passing frequency on boundary layer transition, experimental investigation and wavelet analysis *J. Fluid Eng.* **125** 251–66
[14] Opoka M M and Hodson H P 2008 Experimental investigation of unsteady transition processes on high-lift T106A turbine blades *J. Propul. Power* **24** 424–32
[15] Miller J A and Fejer A A 1964 Transition phenomena in oscillating boundary-layer flows *J. Fluid Mech.* **18** 438
[16] Obremski H J and Fejer A A 1967 Transition in oscillating boundary layer flows *J. Fluid Mech.* **29** 93–111
[17] Romblad J, Ohno D, Würz W and Krämer E 2020 Laminar to turbulent transition at unsteady inflow conditions: wind tunnel measurements at oscillating inflow angle *Notes on Numerical Fluid Mechanics and Multidisciplinary Design XII* (Berlin: Springer) pp 254–64
[18] Yu D O and Kwon O J 2014 Time-accurate aeroelastic simulations of a wind turbine in yaw and shear using a coupled CFD-CSD method *J. Phys. Conf. Ser.* **524** 012046
[19] Li Z, Wen B, Dong X, Peng Z, Qu Y and Zhang W 2020 Aerodynamic and aeroelastic characteristics of flexible wind turbine blades under periodic unsteady inflows *J. Wind Eng. Ind. Aerod.* **197** 104057
[20] Khayatzadeh P and Nadarajah S 2013 Laminar-turbulent flow simulation for wind turbine profiles using the γ-re$_{\theta t}$ transition model *Wind Energy* **17** 901–18
[21] Thiessen R and Schülein E 2019 Infrared thermography and DIT of quadcopter rotor blades using laser heating *15th Int. Workshop on Advanced Infrared Technology and Applications (Basel, Switzerland)* **27** 31
[22] Quast A 2006 Detection of transition by infrared image techniques *Tech. Soaring* **30** 33–8
[23] Carlomagno G, De Luca L, Buresti G and Lombardi G 1988 Characterization of boundary layer conditions in wind tunnel tests through IR thermography imaging *Proc. SPIE Appl. Infrared Tech.* **918** 23–9
[24] de Luca L, Carlomagno G M and Buresti G 1990 Boundary layer diagnostics by means of an infrared scanning radiometer *Exp. Fluids* **9** 121–8
[25] Astarita T and Carlomagno G M 2013 *Infrared Thermography for Thermo-Fluid-Dynamics* (Berlin: Springer)
[26] Joseph L A, Borgoltz A and Devenport W 2016 Infrared thermography for detection of laminar-turbulent transition in low-speed wind tunnel testing *Exp. Fluids* **57** 77
[27] Beeby T, Ackermann J, Langel C M, Chow R, Van Dam C P and Raffius T 2016 A quantitative investigation of surface roughness effects on airfoil boundary layer transition using infrared thermography *54th AIAA Aerosp. Sci. Meet. (San Diego, CA)* (Reston, VA: AIAA)
[28] Yokokawa Y 2005 Transition measurement on metallic aircraft model in typical lowspeed wind tunnel *T. JPN Soc. Aeronaut. S.* **48** 175–6
[29] Hall R M, Obara C J, Carraway D L, Johnson C B, Wright Jr R E and Covell P F 1990 Comparisons of boundary-layer transition measurement techniques at supersonic mach numbers *AIAA J.* **29** 865–71
[30] Zuccher S and Saric W S 2008 Infrared thermography investigations in transitional supersonic boundary layers *Exp. Fluids* **44** 145–57
[31] Crawford B K, Duncan Jr G T West D E and Saric W S 2013 Laminar-turbulent boundary layer transition imaging using IR thermography *Opt. Photo. J.* **3** 233–9
[32] Crawford B K, Duncan Jr G T West D E and Saric W S 2015 Robust, automated processing of IR thermography for quantitative boundary-layer transition measurements *Exp. Fluids* **56** 149
[33] Carlomagno G M and Cardone G 2010 Infrared thermography for convective heat transfer measurements *Exp. Fluids* **49** 1187–1218
[34] Le Sant Y, Marchand M, Millan P and Fontaine J 2002 An overview of infrared thermography techniques used in large wind tunnels *Aerosp. Sci. Technol.* **6** 355–66
[35] Liepmann H W and Skinner G T 1954 Shearing-stress measurements by use of a heated element (NACA: NACA TN 3268)
[36] Bellhouse B J and Schultz D L 1966 Determination of mean and dynamic skin friction, separation and transition in low-speed flow with a thin-film heated element *J. Fluid Mech.* **24** 379–400
[37] Braune M and Koch S 2020 Application of hot-film anemometry to resolve the unsteady boundary layer transition of a laminar airfoil experiencing limit cycle oscillations *Exp. Fluids* **61** 68
[38] Richter K, Koch S, Gardner A D, Mai H, Klein A and Rohardt C H 2014 Experimental investigation of unsteady transition on a pitching rotor blade airfoil *J. Am. Helicopter Soc.* **59** 1–12
[39] Roberts L S, Finnis M V, Knowles K and Lawson N J 2017 Forcing boundary-layer transition on an inverted airfoil in ground effect *J. Aircraft* **54** 2165–72
[40] Sun B, Ma B, Wang P, Luo J, Deng J and Gao C 2020 High sensitive flexible hot-film sensor for measurement of unsteady boundary layer flow *Smart Mater. Struct.* **29** 035023
[41] Schreck S J, Faller W E and Helin H E 1998 Pitch rate and reynolds number effects on unsteady boundary-layer transition and separation *J. Aircraft* **35** 46–52
[42] Lee T and Basu S 1998 Measurement of unsteady boundary layer developed on an oscillating airfoil using multiple hot-film sensors *Exp. Fluids* **25** 108–17
[43] Lee T and Gerontakos P 2004 Investigation of flow over an oscillating airfoil *J. Fluid Mech.* **512** 313–41
[44] Chandrasekhara M S and Wilder M C 2003 Heat-flux gauge studies of compressible dynamic stall *AIAA J.* **41** 757–62
[45] Richter K, Koch S, Goerttler A, Lütke B, Wolf C C and Benkel A 2015 Unsteady boundary layer transition on the

DSA-9A rotor blade airfoil *41st European Rotorcraft Forum (Munich, Germany)*
[46] Richter K, Wolf C C, Gardner A D and Merz C B 2016 Detection of unsteady boundary layer transition using three experimental methods *54th AIAA Aerosp. Sci. Meet. (San Diego, CA USA)* (Reston, VA: AIAA)
[47] Mai H and Hebler A 2011 Aeroelasticity of a laminar wing *15th Int. Forum on Aeroelasticity and Structural Dynamics* (*Paris, France*)
[48] Hebler A 2017 Experimental Assessment of the Flutter Stability of a Laminar Airfoil in Transonic Flow *17th Int. Forum on Aeroelasticity and Structural Dynamics (Como, Italy)*
[49] Lorber P F and Carta F O 1992 Unsteady transition measurements on a pitching three-dimensional wing *The 5th Symp. on Numerical and Physical Aspects of Aerodynamic Flows* (Long Beach, CA: California State University)
[50] Sémézis Y and Beaumier P 1995 Determination de l'Etat de la couche limite sur des sections de Pale d'helicoptere a l'aide de films chauds *Tech. Rep.* onera tap–95-065 ONERA
[51] Schaffarczyk A P, Schwab D and Breuer M 2017 Experimental detection of laminar-turbulent transitionon a rotating wind turbine blade in the free atmosphere *Wind Energy* **20** 210–20
[52] Goerttler A, Gardner A D and Richter K 2017 Chapter Unsteady Boundary Layer Transition Detection by Automated Analysis of Hot Film Data *Numerical and Experimental Fluid Mechanics XI* (Springer Berlin Heidelberg) pp 387–96
[53] Mertens C, Wolf C C, Gardner A D, Schrijer F F J and van Oudheusden B W 2020 Advanced infrared thermography data analysis for unsteady boundary layer transition detection *Meas. Sci. Technol.* **31** 015301
[54] Mee D J 2002 Boundary-layer transition measurements in hypervelocity flows in a shock tunnel *AIAA J.* **40** 1542–8
[55] Boiko A V, Dovgal A V and Sorokin A M 2018 Stability of time-periodic flow with laminar boundary-layer separation *Thermophys. Aeromech.* **25** 667–73
[56] Kato K, Alfredsson P H and Lingwood R J 2019 Boundary-layer transition over a rotating broad cone *Phys. Rev. Fluid* **4** 1–8
[57] Gardner A D and Richter K 2015 Boundary layer transition determination for periodic and static flows using phase-averaged pressure data *Exp. Fluids* **56** 119
[58] Schwermer T 2018 *Experimentelle Untersuchung des dynamischen Strömungsabrisses an einem Rotor mit axialer Zuströmung PhD Thesis* Leibniz University of Hannover
[59] Gardner A D, Wolf C C and Raffel M 2016 A new method of dynamic and static stall detection using infrared thermography *Exp. Fluids* **57** 149
[60] Merz C B, Wolf C C, Richter K, Kaufmann K, Mielke A and Raffel M 2017 Spanwise differences in static and dynamic stall on a pitching rotor blade tip model *J. Am. Helicopter Soc.* **62** 1–11
[61] Gardner A D, Merz C B and Wolf C C 2019 Effect of sweep on a pitching finite wing *J. Am. Helicopter Soc.* **64** 1–13
[62] Schwermer T, Gardner A D and Raffel M 2019 A novel experiment to understand the dynamic stall phenomenon in rotor axial flight *J. Am. Helicopter Soc.* **64** 1–11
[63] Weiss A, Wolf C C, Kaufmann K, Braukmann J N, Heineck J T and Raffel M 2020 Unsteady boundary-layer transition measurements and computations on a rotating blade under cyclic pitch conditions *Exp. Fluids* **61** 61
[64] Gao Y, Zhu Q and Wang L 2016 Measurement of unsteady transition on a pitching airfoil using dynamic pressure sensors *J. Mech. Sci. Technol.* **30** 4571–8
[65] Wei B, Gao Y, Wang L and Li D 2019 Analysis of flow transition and separation on oscillating airfoil by pressure signature *J. Mech. Sci. Technol.* **33** 279–88
[66] Zhang D H, Chew Y T and Winoto S H 1996 Investigation of intermittency measurement methods for transitional boundary layer flows *Exp. Therm. Fluid Sci.* **12** 433–43
[67] Özcakmak O S, Srensen N N, Madsen H A and Srensen J N 2019 Laminar-turbulent transition detection on airfoils by high-frequency microphone measurements *Wind Energy* **22** 1356–70
[68] Reichstein T, Schaffarczyk A P, Dollinger C, Balaresque N, Schülein E, Jauch C and Fischer A 2019 Investigation of laminar–turbulent transition on a rotating wind-turbine blade of multimegawatt class with thermography and microphone array *Energies* **12** 1–21
[69] Liu T and Sullivan J P 2005 *Pressure and Temperature Sensitive Paints* (Berlin: Springer)
[70] Asai K, Kanda H, Kunimasu T, Liu T and Sullivan J P 1997 Boundary-layer transition detection in a cryogenic wind tunnel using luminescent paint *J. Aircraft* **34** 34–42
[71] Gartenberg E and Wright R E 1994 Boundary-layer transition detection with infrared imaging emphasizing cryogenic applications *AIAA J.* **32** 1875–82
[72] Fey U and Egami Y 2007 Transition detection by temperature-sensitive paint *Springer Handbook of Experimental Fluid Mechanics* (Berlin: Springer) pp 537–52
[73] Lang W, Gardner A D, Mariappan S, Klein C and Raffel M 2015 Boundary-layer transition on a rotor blade measured by temperature-sensitive paint *thermal imaging and image derotation. Exp. Fluids* **56** 118
[74] Weiss A, Gardner A D, Klein C and Raffel M 2017 Boundary-layer transition measurements on mach-scaled helicopter rotor blades in climb *CEAS Aeronaut.* J. **8** 613–23
[75] Yorita D, Lemarechal J, Klein C, Fujita K and Nagai H 2020 Transition detection methods in a pitch-sweep test by means of TSP using lifetime and intensity measurements *AIAA Scitech Forum (Orlando, FL, USA)* (Reston, VA: AIAA)
[76] Goyne C P, Stalker R J and Paull A 2003 Skin-friction measurements in high-enthalpy hypersonic boundary layers *J. Fluid Mech.* **485** 1–32
[77] Schetz J 2010 Direct measurement of skin friction in complex flows *48th AIAA Aerospace Sciences Meeting Including the New Horizons Forum and Aerospace Exposition* (*Orlando, FL, USA*)
[78] Chen X, Bi Z X, Gong J, Yao D P and Wen S 2012 Optical skin friction measurement using shear-sensitive liquid-crystal coatings *J. Experiments in Fluid Mechanics* **26** 70–4
[79] Horstmann K H, Quast A and Redeker G 1990 Flight and wind-tunnel investigations on boundary-layer transition *J. Aircraft* **27** 146–50
[80] Wolf C C, Mertens C, Gardner A D, Dollinger C and Fischer A 2019 Optimization of differential infrared thermography for unsteady boundary layer transition measurement *Exp. Fluids* **60** 19
[81] Simon B, Filius A, Tropea C and Grundmann S 2016 IR thermography for dynamic detection of laminar turbulent transition *Exp. Fluids* **57** 93
[82] Richter K and Schülein E 2014 Boundary-layer transition measurements on hovering helicopter rotors by infrared thermography *Exp. Fluids* **55** 1755
[83] Overmeyer A D and Martin P B 2017 Measured boundary layer transition and rotor hover performance at model scale *55th AIAA Aerospace Sciences Meeting, AIAA SciTech Forum (Grapevine, TX, USA)*

[84] Klein C and Henne U 2015 Combination of temperature sensitive paint and carbon nanotubes for transition detection *53rd AIAA Aerospace Sciences Meeting (Kissimmee, FL, USA)* (Reston, VA: AIAA)
[85] Richter K, Schülein E, Ewers B, Raddatz J and Klein A 2016 Boundary layer transition characteristics of a full-scale helicopter rotor in hover *72nd Annual Forum of the American Helicopter Society (West Palm Beach, FL, USA)*
[86] Grawunder M, Reß R and Breitsamter C 2016 Thermographic transition detection for low-speed wind-tunnel experiments *AIAA J.* **54** 2011–15
[87] Costantini M, Fey U, Henne U and Klein C 2015 Nonadiabatic surface effects on transition measurements using temperature-sensitive paints *AIAA J.* **53** 1172–87
[88] Boden F, Stasicki B, Szypula M, Ružička P, Tvrdik Z and Ludwikowski K 2016 In-flight measurements of propeller blade deformation on a VUT100 cobra aeroplane using a co-rotating camera system *Meas. Sci. Technol.* **27** 074013
[89] Boden F, Stasicki B and Ludwikowski K 2018 Optical rotor-blade deformation measurements using a rotating camera *European Test and Telemetry Conf. (Nuremberg, Germany)*
[90] Waddle C E, Bolan J T, Dobbins C L, Hall Z M and McDaniel M A 2018 Visualization and analysis of boundary layer transitions using infrared thermography *Proc. SPIE, Thermosense: Thermal Infrared Applications XL* **10661** 1–18
[91] Dollinger C, Balaresque N, Gaudern N, Gleichauf D, Sorg M and Fischer A 2019 Ir thermographic flow visualization for the quantification of boundary layer flow disturbances due to the leading edge condition *Renew. Energ.* **138** 709–21
[92] Doroshtnasir M, Worzewski T, Krankenhagen R and Röllig M 2016 On-site inspection of potential defects in wind turbine rotor blades with thermography *Wind energy* **19** 1407–22
[93] Raffel M and Heineck J T 2014 Mirror-based image derotation for aerodynamic rotor measurements *AIAA J.* **52** 1337–41
[94] Overmeyer A, Heineck J T and Wolf C C 2018 Unsteady boundary layer transition measurements on a rotor in forward flight *74th Annu. Forum of the Am. Helicopter Soc. (Phoenix, AZ USA)*
[95] Heineck J T, Schairer E T, Rozeboom N H and Ramasamy M 2016 Simultaneous boundary-layer transition, tip vortex and blade deformation measurements of a rotor in hover *AHS Technical Meeting on Aeromechanics Design for Vertical Lift (San Francisco, CA USA)*
[96] Theodorsen T 1949 General theory of aerodynamic instability and the mechanism of flutter (NACA: NACA TR 496)
[97] Szewczyk M, Smusz R, de Groot K, Meyer J, Kucaba-Pietal A and Rzucidlo P 2017 In-flight investigations of the unsteady behaviour of the boundary layer with infrared thermography *Meas. Sci. Technol.* **28** 044002
[98] Raffel M and Merz C B 2014 Differential infrared thermography for unsteady boundary-layer transition measurements *AIAA J.* **52** 2090–3
[99] Raffel M, Merz C B, Schwermer T and Richter K 2015 Differential infrared thermography for boundary layer transition detection on pitching rotor blade model *Exp. Fluids* **56** 30
[100] Ikami T, Fujita K, Nagai H and Yorita D 2020 Easurement of boundary layer transition on oscillating airfoil using cnttsp in low-speed wind tunnel *AIAA Scitech Forum (Orlando, FL, USA)* (Reston, VA: AIAA)
[101] Gardner A D, Eder C, Wolf C C and Raffel M 2017 Analysis of differential infrared thermography for boundary layer transition detection *Exp. Fluids* **58** 122
[102] von Hoesslin S, Stadlbauer M, Gruendmayer J and Kähler C J 2017 Temperature decline thermography for laminar–turbulent transition detection in aerodynamics *Exp. Fluids* **58** 129
[103] Gardner A D and Richter K 2016 Transition determination on a periodic pitching airfoil using phase averaging of pressure data *Notes on Numerical Fluid Mechanics and Multidisciplinary Design X* pp 291–301 (Berlin: Springer)
[104] Mertens C, Wolf C C and Gardner A D 2019 Unsteady boundary layer transition detection with local infrared thermography *Notes on Numerical Fluid Mechanics and Multidisciplinary Design XII* pp 382–91 (Berlin: Springer)
[105] Weiss A, Gardner A D, Schwermer T, Klein C and Raffel M 2019 On the effect of rotational forces on rotor blade boundary-layer transition *AIAA J.* **57** 252–66
[106] Kaufmann K, Ströer P, François Richez C Gardarein L, P, Krimmelbein N and Gardner A D 2019 Validation of boundary-layer-transition computations for a rotor with axial inflow *75th Annual Forum of the American Helicopter Society* (*Philadelphia, PA, USA*)
[107] Gardner A D, Wolf C C, Heineck J T, Barnett M and Raffel M 2020 Helicopter rotor boundary layer transition measurement in florward flight using an infrared camera *J. Am. Helicopter Soc.* **65** 1–13
[108] Gartenberg E and Roberts Jr A S 1991 Airfoil transition and separation studies using an infrared imaging system *J. Aircraft* **28** 225–30
[109] Montelpare S and Ricci R 2004 A thermographic method to evaluate the local boundary layer separation phenomena on aerodynamic bodies operating at low reynolds number *Int. J. Therm. Sci.* **43** 315–29
[110] Raffel M, Gardner A D, Schwermer T, Merz C B, Weiss A, Braukmann J and Wolf C C 2017 Rotating blade stall maps measured by differential infrared thermography *AIAA J.* **55** 1753–6